

The Spitzer Spirals, Bridges, and Tails Interacting Galaxy Survey: Interaction-Induced Star Formation in the Mid-Infrared

Beverly J. Smith

Department of Physics, Astronomy, and Geology, East Tennessee State University, Johnson City TN 37614
smithbj@etsu.edu

Curtis Struck

Department of Physics and Astronomy, Iowa State University, Ames IA 50011
curt@iastate.edu

Mark Hancock

Department of Physics, Astronomy, and Geology, East Tennessee State University, Johnson City TN 37614
hancockm@etsu.edu

Philip N. Appleton

Spitzer Science Center, California Institute of Technology, Pasadena CA 91125
apple@ipac.caltech.edu

Vassilis Charmandaris¹

Department of Physics, University of Crete, GR-71003, Heraklion, Greece
vassilis@physics.uoc.gr
and

William T. Reach

Spitzer Science Center, California Institute of Technology, Pasadena CA 91125
reach@ipac.caltech.edu

ABSTRACT

We present Spitzer mid-infrared imaging of a sample of 35 tidally-distorted pre-merger interacting galaxy pairs selected from the Arp Atlas. We compare their global mid-infrared properties with those of normal galaxies from the SINGS Spitzer Legacy survey, and separate the disk emission from that of the tidal features. The $[8.0 \mu\text{m}] - [24 \mu\text{m}]$, $[3.6 \mu\text{m}] - [24 \mu\text{m}]$, and $[5.8 \mu\text{m}] - [8.0 \mu\text{m}]$ colors of these optically-selected interacting galaxies are redder on average than those of spirals, implying enhancements to the mass-normalized star formation rates (SFRs) of a factor of ~ 2 . Furthermore, the $24 \mu\text{m}$ emission in the Arp galaxies is more centrally concentrated than that in the spirals, suggesting that gas is being concentrated into the inner regions and fueling central star formation. No significant differences can be discerned in the shorter wavelength Spitzer colors of the Arp galaxies compared to the spirals, thus these quantities are less sensitive to star formation enhancements. No strong trend of Spitzer color with pair separation is visible in our sample; this may be because our sample was selected to be tidally disturbed. The tidal features contribute $\leq 10\%$ of the total Spitzer fluxes on average. The SFRs implied for the Arp galaxies by the Spitzer $24 \mu\text{m}$ luminosities are relatively modest, $\sim 1 M_{\odot} \text{ yr}^{-1}$ on average.

Subject headings: galaxies: starbursts — galaxies: interactions — galaxies: infrared

1. Introduction

Since the early work of Larson & Tinsley (1978) and Struck-Marcell & Tinsley (1978), there has been a great deal of interest in how star formation in galaxies is affected by collisions with other galaxies. Infrared Astronomical Satellite (IRAS) observations led to the discovery of galaxies with very high far-infrared luminosities (Soifer et al. 1987; Smith et al. 1987) that are the result of mergers between equal-mass gas-rich progenitors (Sanders et al. 1988). Many studies since that time have shown that spectacular and prolonged enhancement of star formation is the cause of much of the infrared emission in major mergers (see reviews by Sanders & Mirabel 1996 and Struck 1999).

The question of how star formation is affected in interacting galaxies before a merger occurs is subtle and more difficult to answer. Since dynamical models of interactions suggest that the pre-merger stage is relatively long-lived, understanding the properties of nearby interacting galaxies and their differences from field spirals is important in interpreting the results of high redshift surveys (e.g., Le Fèvre et al. 2000; Bundy et al. 2004). Early studies indicated that on average the $H\alpha$ equivalent widths and far-infrared-to-blue luminosity ratios in both close pairs and in morphologically-peculiar Arp (1966) Atlas interacting galaxies are enhanced by about a factor of two relative to those of spiral galaxies, with more disturbed systems tending to have higher values (Bushouse 1987; Bushouse, Lamb, & Werner 1988; Kennicutt et al. 1987). There is, however, a large scatter in these values, with many interacting galaxies having SFRs typical of normal spirals. Star formation enhancement appears to be a function of pair separation, with pairs closer than ~ 30 kpc having higher $H\alpha$ equivalent widths on average than wider pairs (Barton et al. 2000; Lambas et al. 2003; Nikolic, Cullen, & Alexander 2004). However, there is much scatter in this relationship, with many close pairs having low $H\alpha$ equivalent widths. In many cases, star formation is enhanced in the nuclear regions compared to the disks (Hummel et al. 1990; Nikolic, Cullen,

& Alexander 2004). Although luminous star formation regions have been found in tidal tails and bridges (e.g., Schweizer 1978; Mirabel et al. 1991, 1992), the optical broadband colors of tidal features are often similar to those of outer disks, but with a larger scatter (Schombert, Wallin, & Struck-Marcell 1990).

To date, most studies comparing interacting galaxies to normal galaxies have been based on optical data, which suffer from extinction, or IRAS far-infrared data. The limited spatial resolution of IRAS, however, provided only a global measurement of the far-infrared luminosities of all but the most nearby galaxies; furthermore, dust heating by the older stellar population may also contribute to the far-infrared luminosities (e.g., Persson & Helou 1987; Smith et al. 1991, 1994). An alternative tracer of star formation is the mid-infrared, given the close coupling between HII regions and the surrounding photodissociation regions, which emit strongly in the mid-infrared (see Hollenbach & Tielens 1997). Observations with the Infrared Space Observatory (ISO) revealed direct correlations between the $H\alpha$ luminosity, the mid-infrared dust features, and the mid-infrared continuum fluxes in galaxies (Roussel et al. 2001; Helou et al. 2001; Förster Schreiber et al. 2004).

With the advent of the Spitzer Space Telescope (Werner et al. 2004), mid-infrared imaging of galaxies entered a new era. The large format mid-infrared detector arrays of Spitzer, nearly two orders of magnitude more sensitive than those of ISO, make feasible the detailed study of individual star formation complexes in nearby galaxies (e.g., Calzetti et al. 2005; Smith et al. 2005; Elmegreen et al. 2006; Hancock et al. 2006). Spitzer is well-suited for studying induced star formation in spiral arms and tidal bridges and tails, and detecting knots of star formation (see Smith et al. 2005).

In the current paper, we present results from a Spitzer mid-infrared survey of a well-defined sample of nearby interacting galaxy pairs. We discuss the global infrared properties of the galaxies in our sample, and compare them with those of normal spiral, elliptical/S0, and irregular galaxies. We also compare the infrared colors of the main disks with those of the tidal features in these galaxies. Detailed studies of clumps of star formation in two of the galaxies in our sample, Arp 107 and Arp 82, are presented in Smith et al. (2005) and Hancock

¹Chercheur Associé, Observatoire de Paris, F-75014, Paris, France, and IESL/Foundation for Research and Technology-Hellas, PO Box 1527, 71110, Heraklion, Greece

et al. (2006).

2. The Samples

2.1. The Interacting Galaxy Sample

Our interacting galaxy sample was selected from the Arp Atlas of Peculiar Galaxies (Arp 1966), based on the following criteria: 1) They are relatively isolated binary systems; we eliminated merger remnants and close triples and multiple systems in which the galaxies have similar optical brightnesses (systems with additional smaller angular size companions were not excluded). 2) They are tidally disturbed. 3) They have radial velocities less than 11,000 km/s (150 Mpc, for $H_0 = 75 \text{ km s}^{-1} \text{ Mpc}^{-1}$). 4) Their total angular size is $> 3'$ and the angular sizes of the individual galaxies are $\geq 30''$, to allow for good spatial resolution with Spitzer. A total of 35 Arp systems fit these criteria. One of these systems, Arp 297, consists of two pairs at different redshifts. These two pairs are included separately in our sample. We also include the interacting pair NGC 4567, which fits the above criteria but is not in the Arp Atlas. This brings the sample to 37.

Of these 37 systems, 28 were included in our ‘Spirals, Bridges, and Tails’ (SB&T) Guest Observer Cycle 1 Spitzer program. The remaining nine galaxies were reserved as part of various Guaranteed Time or Guest Observer programs. For completeness, in our survey we included the seven of these additional galaxies for which the data were publicly-available. This brings our final sample size to 35 pairs.

The 35 galaxy pairs in our sample are listed in Table 1, in order of their number in the Arp Atlas. Table 1 also includes alternative names for the galaxies, notes on the optical morphologies of the systems based on the Arp (1966) photographs, as well as the nuclear optical spectral type when available from Keel et al. (1985) or Dahari (1985). The interacting sample contains three known Seyferts and 13 Low Ionization Emission Line (LINER) galaxies (4% and 19%, respectively). The distances given in Table 1 were calculated using velocities from the NASA Extragalactic Database (NED), a Hubble constant of $75 \text{ km s}^{-1} \text{ Mpc}^{-1}$, and the Schechter (1980) Virgocentric infall model with parameters as in Heckman et al. (1998). A histogram of the distances is

shown in the top panel of Figure 1. The median distance is 47 Mpc and the maximum distance is 143 Mpc.

Table 1 also includes far-infrared luminosities ($40 - 120 \mu\text{m}$), when available, calculated² as in Lonsdale et al. (1985) and Persson & Helou (1987) using IRAS fluxes obtained from Sanders et al. (2003), the IRAS Faint Source Catalog (Moshir et al. 1992), or the *scanpi* software³. A histogram of these luminosities is shown in the top panel of Figure 2.

2.2. The ‘Normal’ Galaxy Sample

As a ‘control’ sample of nearby ‘normal’ galaxies, we started with the 75 galaxies in the Spitzer Infrared Nearby Galaxies Survey (SINGS) (Kennicutt et al. 2003; Dale et al. 2005). The SINGS sample was selected to cover a wide range in parameter space, with a wide range in Hubble type and luminosity. Most objects have angular sizes between $5'$ and $15'$.

We used the NASA Extragalactic Database (NED⁴) to search for companions to the SINGS galaxies. We eliminated from our ‘normal’ sample galaxies with companions whose velocities differ from that of the target galaxy by $\leq 1000 \text{ km s}^{-1}$, have an optical luminosity brighter than 1/10th of that of the target galaxy, and are separated from the target galaxy by less than 10 times the optical diameter of the target galaxy or the companion, whichever is larger. We emphasize that our ‘normal’ galaxies are not necessarily completely isolated; some have distant or low mass companions. However, they are not subject to the strong perturbing forces of the Arp sample. For comparison, the Large Magellanic Cloud has an optical luminosity $\sim 1/9$ th that of the Milky Way (van den Bergh 2000), thus our ‘normal’ galaxies are less perturbed than the Milky Way. We note that three of the galaxies eliminated from the ‘normal’ sample by this method had previously been in-

² $L_{FIR}(L_{\odot}) = 3.94 \times 10^5 D^2 (2.58 F_{60} + F_{100})$, where D is the distance in Mpc and F_{60} and F_{100} are the IRAS 60 and 100 μm flux densities in Jy.

³http://irsa.ipac.caltech.edu/IRASdocs/scanpi_over.html

⁴The NASA/IPAC Extragalactic Database (NED) (<http://nedwww.ipac.caltech.edu>) is operated by the Jet Propulsion Laboratory, California Institute of Technology, under contract with the National Aeronautics and Space Administration.

cluded in the interacting sample: NGC 2798 (Arp 283), NGC 5194, and NGC 5195 (Arp 85 = M51). A total of 42 SINGS galaxies remain in our ‘normal’ galaxy sample; of these, 26 are spirals, 4 are ellipticals or S0s, and 12 are irregulars/Sm. These galaxies are listed in Table 2. These three groups are treated separately in our analysis below.

Table 2 also includes the distances, Hubble types, and far-infrared luminosities for the sample galaxies. As shown in Figure 1, these ‘normal’ galaxies are more nearby than our interacting sample, with median and maximum distances of 9.6 Mpc and 25 Mpc, respectively.

The mean and median far-infrared luminosities L_{FIR} for the various samples are given in Table 3. Table 3 also includes the mean, median, and rms of the total 8 – 1000 μm infrared luminosity L_{IR} , calculated using the relationship in Perault (1987), Sanders & Mirabel (1996), and Kennicutt (1998). A histogram of the far-infrared luminosities is given in Figure 2. After dividing the Arp luminosities by a factor of two, to account for the two disks in the pair, a Kolmogorov-Smirnov (KS) test cannot rule out that the spiral and Arp luminosities come from the same parent distribution. Although the distributions are similar, the median far-infrared luminosity for the Arp galaxies, per disk, is slightly larger than that of the spirals, a factor of ~ 2 , consistent with the results of Bushouse, Lamb, & Werner (1988) for a similar optically-selected sample.

3. Observations and Data Reduction

The galaxies in our SB&T sample were observed between November 2004 and August 2005 in the 3.6, 4.5, 5.8 and 8.0 μm broadband filters of the Spitzer Infrared Array Camera (IRAC; Fazio et al. 2004) and the 24 μm band of the Multiband Imaging Photometer for Spitzer (MIPS; Rieke et al. 2004). For the IRAC observations, we used 12 sec frames in a cycling dither pattern, with between 4 and 23 positions per system. Most galaxies had a small enough angular size to fit within the $5' \times 5'$ field of view of IRAC, or could be imaged with a small map. The exceptions were NGC 4567, Arp 82, Arp 89, and Arp 279, for which two pointings were necessary. For the MIPS observations, we used fixed single observations with two cycles of 10 sec integrations per frame, resulting

in an on-source time of 312.5 sec per target. The details of the SB&T observations are presented in Table 4.

We started our analysis of the 3.6 μm and 4.5 μm interacting galaxy data with the version S13.2.0 post-pipeline Basic Calibrated Data (post-BCD) mosaicked images. At 5.8 μm , 8.0 μm , and 24 μm , the pipeline post-BCD mosaicked images show significant artifacts in the sky background, in particular, ‘boxiness’ due to imperfect matching of sky levels between images during mosaicking. Therefore, for these wavelengths we started with the S13.2.0 BCD images and mosaicked them ourselves using the MOPEX⁵ software. We first ran an overlap correction using a drizzle interpolation method with a drizzle factor of 1, and then ran the mosaicking module. In addition, at 5.8 μm and 8.0 μm , bright point sources in some of the images (often the nuclei of the galaxies) cause horizontal ‘bands’ in the images (‘muxbleed’). These were removed by interpolation from nearby clean areas. Furthermore, a strong ‘sky’ gradient was present in some of the mosaicked images. To remove this gradient, we used the Image Reduction and Analysis Facility (IRAF⁶) routine *imsubfit* to fit and subtract the background. For the SINGS galaxies, we started with the SINGS Data Release 4 mosaicked images⁷. When necessary, we subtracted a gradient from the SINGS images.

The final 3.6 μm , 8.0 μm , and 24 μm images for the interacting galaxy sample are shown in Figures 3 – 11, ordered by their Arp number. From these and the SINGS images, at each wavelength we determined flux densities for each disk and tidal feature. We used multiple rectangular boxes that cover the entire observed extent of these features in the 3.6 μm images, avoiding bright foreground stars and their residuals. These same regions were then used for the other wavelength images. Multiple blank sky fields away from the galaxies were measured for sky subtraction. We avoided the edges of the images in selecting sky regions, due to edge effects in the final images.

⁵<http://ssc.spitzer.caltech.edu/postbcd/download-mopex.html>

⁶IRAF is distributed by the National Optical Astronomy Observatories, which are operated by the Association of Universities for Research in Astronomy, Inc., under cooperative agreement with the National Science Foundation.

⁷See <http://ssc.spitzer.caltech.edu/legacy>

The final flux densities for the Arp galaxies are tabulated in Table 5, while those for the SINGS galaxies are given in Table 6. The quoted upper limits are 3σ . The uncertainties given in Tables 5 and 6 and used to calculate upper limits are a combination of statistical uncertainties and uncertainties in the sky subtraction due to inhomogeneities and residual sky gradients in the final mosaicked images. For the sky regions in an image, we calculated the mean rms noise $\langle rms \rangle$ and the rms of the mean sky $rms_{\langle sky \rangle}$, where $rms_{\langle sky \rangle}$ is the standard deviation of the means of the different sky regions in an image. The quantity $rms_{\langle sky \rangle}$ is a measure of the ‘flatness’ of the final image, i.e., the artifacts in the background. The uncertainties, σ , quoted in Tables 5 and 6 and used in the subsequent figures were calculated using $\sigma^2 = (\langle rms \rangle * \sqrt{N})^2 + (rms_{\langle sky \rangle} * N)^2$, where N is the number of pixels in the galaxy apertures in question. The first term in this equation is the standard statistical uncertainty, while the second term is a measure of the uncertainty due to variations in the sky level across the image. The latter term typically dominates by a factor of ~ 9 . The median uncertainty in Table 5 is $\sim 3\%$, with 80% of the sources having uncertainties $\leq 10\%$. The sky artifacts are worse at $5.8 \mu\text{m}$ and $24 \mu\text{m}$ than at the other wavelengths, thus these two bands have the most upper limits quoted in Tables 5 and 6. Note that our upper limits are quite conservative; in some cases, galaxies are visible in the image but sky problems prevent an accurate flux from being determined.

The uncertainties given in Tables 5 and 6 do not include absolute calibration uncertainties, which are $\leq 10\%$ (IRAC Data Manual; MIPS Data Manual). Additional uncertainties arise from ambiguities in selecting the boundaries of the galaxy and sky regions, possible contributions from foreground stars inadvertently included in the galaxy region, and the mosaicking process. Our fluxes for the SINGS galaxies typically agree within 10 – 20% with those determined independently by Dale et al. (2005). This provides an upper limit to these additional uncertainties.

In the $24 \mu\text{m}$ images of some of the galaxies with very bright galactic nuclei, the MIPS point spread function (see MIPS Data Handbook) is visible as a ring around the nucleus, and six radial spikes extending out from the nucleus (see Arp 84, 87, 104,

181, 242, 283, 284, 295, 297, and 298 in Figures 4 – 10). In these systems, accurate measurement of $24 \mu\text{m}$ tidal flux densities are not possible.

4. Global Spitzer Luminosities

In Figures 12, 13, and 14, we present histograms of the $3.6 \mu\text{m}$, $8.0 \mu\text{m}$, and $24 \mu\text{m}$ luminosities, respectively, for the various classes of galaxies. In Table 7, we give the median, mean, and rms $3.6 \mu\text{m}$, $8.0 \mu\text{m}$, and $24 \mu\text{m}$ luminosity for each class. As with the far-infrared luminosities, at all three Spitzer wavelengths KS tests cannot rule out that the Arp and spiral luminosities originated from the same parent distribution.

The $3.6 \mu\text{m}$ luminosity provides an approximate measure of the stellar mass in the galaxy. At this wavelength, the distribution for the Arp disks extends to lower luminosities than that of spirals, and has a slightly lower mean luminosity than the spiral galaxies. This is likely because of the inclusion of low mass companions, which in some cases may have originally been irregular or dwarf elliptical galaxies. At $8 \mu\text{m}$ and $24 \mu\text{m}$, the Arp distributions are similar to those of spirals, however, as at $3.6 \mu\text{m}$, there is a tail of lower luminosity, low mass galaxies, compared to spirals. There is also a slight excess of higher luminosity Arp disks at $24 \mu\text{m}$. The median $24 \mu\text{m}$ luminosity for the Arp disks is slightly higher ($\sim 1.8\times$) that of the spirals.

As expected, the luminosities of the irregular galaxies are typically less than those of the spirals. The luminosities of the tails and bridges also tend to be lower than those of the Arp disks on average, as expected. The tidal features tend to be more luminous than the irregular galaxies, overlapping in luminosities with the spirals to some extent. This is probably due in part to contributions from the underlying disks, and in part due to a selection effect, as these systems were selected for having prominent tidal features. On average, the $3.6 \mu\text{m}$ luminosities (and therefore the stellar masses) of the tidal features are $\sim 7\%$ that of the Arp disks (see Table 7). The fractional fluxes in the tidal features are similar at the other Spitzer wavelengths. We note that there is some uncertainty in defining ‘tidal’ vs. ‘disk’ regions; for example, in some systems, large star formation regions lie at the base of a tidal feature. Generally mid-infrared-bright extra-nuclear star formation regions in the vicin-

ity of the main galaxies are considered ‘disk’ rather than ‘tidal’, but this separation is rather subjective.

5. Global Spitzer Colors

In Figure 15, we plot the Spitzer IRAC [3.6] – [4.5] color against the [4.5] – [5.8] color for the main disks (black circles) and tidal features (filled blue triangles) of the galaxies in the interacting sample. In Figure 16, we present the same plot for the SINGS galaxies (spirals: black circles; irregular/Sm: open blue circles; E/S0: open magenta diamonds). In Figures 17 and 18, the [4.5] – [5.8] vs. [5.8] – [8.0] colors for the Arp and SINGS samples, respectively, are plotted. Figures 19 and 20 show the [5.8] – [8.0] vs. [8.0] – [24] colors for the Arp and SINGS galaxies, respectively. No color corrections were included in making these plots. The colors of M0III stars (open magenta square; M. Cohen 2005, private communication), field stars (magenta triangle; Whitney et al. 2004), and predicted IRAC colors of interstellar dust (Li & Draine 2001) are also included in these plots. The Hatziminaoglou et al. (2005) colors of quasars are also plotted (red circles). In calculating magnitudes at 3.6 μm , 4.5 μm , 5.8 μm , 8.0 μm , and 24 μm , we used zero points of 280.9 Jy, 179.7 Jy, 115.0 Jy, 64.1 Jy, and 7.14 Jy, respectively (IRAC Data Manual; MIPS Data Manual).

Histograms showing the distribution of Spitzer colors for the different samples are shown in Figures 21 – 26. In addition to histograms for all of the Arp galaxies, we plot separately the colors for the eight M51-like systems identified in Table 1. Our results are quantified in Table 8, where we provide the mean, median, and rms spread in the Spitzer colors for the different samples. For comparison with Table 8, the mean [3.6] – [4.5], [4.5] – [5.8], [5.8] – [8.0], and [3.6] – [8.0] colors in the Whitney et al. (2004) field stars are -0.05 , 0.1 , 0.05 , and 0.1 , respectively, and the predicted values for interstellar dust are -0.35 , 3.2 , 2.1 , and 4.95 , respectively (Li & Draine 2001). The expected [8.0] – [24] color for dust varies from 2.6 – 4.3 (Li & Draine 2001), increasing with increasing interstellar radiation field intensity, while stars are expected to be at ~ 0.0 . In Figures 21 – 26, the expected colors for stars and dust are indicated by vertical lines.

Results of KS tests for whether these samples were drawn from the same parent sample are given in Table 9. We ran up to three different KS tests per comparison. First, we did a KS test ignoring the upper/lower limits, if any. Then, if these results suggest that the samples are significantly different, we ran another test assuming the limits were detections. Third, if the upper/lower limits were above/below the peak of the comparison sample, to force the best possible match between the samples, we treated the limits as detections near the peak of the comparison sample.

The [3.6] – [4.5] colors for all of the samples tend to lie near 0.0, indicating that these bands are generally dominated by starlight. No significant differences can be discerned between the Arp galaxies and the spirals in this color. The [4.5] – [5.8], [5.8] – [8.0], and [3.6] – [8.0] colors show a relatively wide range, between those expected for stellar photospheres and those of interstellar dust (see Figures 22 – 24). In the [4.5] – [5.8] and [3.6] – [8.0] colors, the mean and median colors the spirals and Arp disks are similar, and KS tests cannot rule out that the spirals and Arp galaxies were drawn from the same sample (see Tables 8 and 9).

In contrast to these shorter wavelength colors, there are statistically significant differences between the [8.0] – [24], [3.6] – [24], and [5.8] – [8.0] colors of the Arp galaxies and those of the spirals, with the Arp galaxies being redder (see Figures 23, 25, and 26, and Tables 8 and 9). The M51-like subset of the Arp galaxies also shows possible differences from the spirals in these colors, however, the M51 sample size is small so these results are tentative.

In the histograms of the colors of the Arp galaxies (Figures 21 – 26), we have distinguished between the more and less massive galaxies in the pair. No significant difference is seen between these two groups.

In most cases, our sample sizes are too small and/or there are too many upper limits to draw strong conclusions about the colors of the irregular/Sm galaxies, the E/S0 galaxies, or the tidal features compared to the spirals or Arp disks. However, we do find a significant difference between the [3.6] – [8.0] colors of irregular/Sm galaxies compared to the spirals, with the Irr/Sm galaxies being bluer. Furthermore, the [3.6] – [4.5]

colors of the Irr/Sm galaxies tend to be redder than those of the other samples.

6. Separation vs. IR colors

To search for correlations between star formation rates and interaction stage, in Figures 27 and 28 we plotted pair separation against the [3.6] – [8.0] and [8.0] – [24] colors. To distinguish between equal mass galaxy pairs and unequal mass pairs, using the 3.6 μm luminosity ratio as a proxy for mass ratio we have separated the galaxies into three groups. The first group (filled black triangles) represent pairs with approximately equal mass (i.e., 3.6 μm luminosity ratios greater or equal to 0.75). The second group, with intermediate mass ratios (3.6 μm luminosity ratios between 0.1 – 0.75) is plotted with red and blue open circles (more and less massive galaxy in the pair, respectively). Pairs with 3.6 μm luminosity ratios less than 0.1 are marked as magenta and green open diamonds, respectively, for the more and less massive galaxy in the pair. These plots show large scatter, without a strong correlation. Plots of the other colors (not shown) show similar scatter, for both the disks and the tidal features.

As an alternative test for whether separation correlates with Spitzer color, we have binned the Arp galaxies into two groups: those with separations less than 30 kpc, and wider pairs. In Figures 29 – 34, we display histograms of the Spitzer colors for these two groups. Mean and median colors for these two groups are given in Table 8, while the results of KS comparison tests are given in Table 9. No significant difference between the wide and close pairs is seen. Although the reddest disks tend to be closer pairs, there is a large amount of scatter, and this result is not statistically significant. The KS test cannot rule out the possibility that the colors of the two samples come from the same parent population.

7. Central Concentration

Unlike IRAS studies, which had limited spatial resolution, Spitzer allows us to look for differences in the spatial distribution of the infrared emission between our samples. To investigate whether the Arp pairs have more centrally concentrated star formation, we have evaluated the 24 μm nuclear emission in a region of diameter 2 kpc centered

on the position of the 2MASS K-band nucleus of each galaxy. The aperture sizes used were calculated using the assumed distances to each galaxy given in Tables 1 and 2. We choose a diameter of 2 kpc so that the central part of the point spread function at 24 μm would subtend at least 2 pixels ($\sim 5''$) for even the most distant members of the sample. We define the nuclear concentration C_{24} to be the ratio of the flux in the aperture $S_{2\text{ kpc}}$ to the total flux S_{tot} from the galaxy.

Since the MIPS point spread function contains considerable power outside the inner peak, we apply an aperture correction to the flux measured in our small nuclear aperture to estimate the contribution from an unresolved nuclear point source to the extended disk. For the pixels scales in the Arp galaxy images ($2.5'' \text{ pixel}^{-1}$) and the SINGs images ($1.5'' \text{ pixel}^{-1}$) we tabulated the correction factors using a high dynamic range map provided by the MIPS team at the Spitzer Science Center. We note that because we assume a point source for the aperture correction, the concentration C_{24} will represent a theoretical lower limit to the actual concentration. The values of C_{24} should therefore be treated as limiting cases where the emission is a true point source at the galaxy center. We performed tests of our aperture correction using some galaxies with pure point sources, and found that it was capable of reproducing the correct flux in the extended PSF to within 5%, even for the smallest aperture. The correction factors range from values of 2.96 in the most extreme cases, to more typically 1.5 for the Arp sample, and 1.1 for the normal galaxy sample. We carefully investigated any redshift-dependent systematic trends of the correction factor on the derived value of C_{24} , and found none. Hence we believe that the values of C_{24} are measured reliably for the Arp and SINGs sample, despite differences in redshift between the two samples.

In Figure 35 we present the distribution of measured values of C_{24} for the spirals and the Arp disks. We bin the value of C_{24} in increments of 0.1 from 0 (no nuclear flux) to 1 (pure point source). The values for the Arp primary and secondary pair members as well as the combined Arp galaxies are shown as separate curves. The vertical axis is the fraction of the total population that falls within each concentration bin.

Figure 35 shows a clear difference in the distri-

bution of $24\ \mu\text{m}$ nuclear concentrations between the spirals and the Arp systems. The spirals are predominantly diffuse objects with the median value of C_{24} being around 0.2 (i.e., 20% of the flux coming from the inner 2kpc) and only tiny fraction of the systems having nuclear concentrations, whereas the Arp systems show an almost flat (and slowly declining) distribution of C_{24} . In particular, large numbers of Arp systems (both primary and secondary galaxies) have values of C_{24} greater than 0.3 and in some cases are totally nuclear dominated. We therefore conclude that Arp systems show a much wider distribution of MIPS $24\ \mu\text{m}$ nuclear concentrations, with a large excess (over the spirals) extending up to objects which are essentially point sources (e.g., the minor component of Arp 89). No strong correlation is seen between the $[3.6] - [24]$ and $[8.0] - [24]$ colors and the central concentration for the Arp galaxies, although the reddest galaxies tend to be somewhat more centrally concentrated.

8. Discussion

8.1. Spitzer Colors and Mass-Normalized Star Formation Rates

To search for interaction-enhanced star formation in the mid-infrared, instead of comparing luminosities, which measure the absolute SFR, it is better to compare Spitzer colors, which measure mass-normalized SFRs. The $[4.5] - [5.8]$, $[3.6] - [8.0]$, $[8.0] - [24]$, and $[3.6] - [24]$ colors are all measures of the mass-normalized SFR, with a redder color indicating a higher normalized SFR (e.g., Smith et al. 2005). The $3.6\ \mu\text{m}$ and $4.5\ \mu\text{m}$ bands are dominated by the older stellar population, while the other bands have significant contributions from interstellar dust heated by young stars.

The $[3.6] - [4.5]$, $[4.5] - [5.8]$, and $[3.6] - [8.0]$ colors of our optically-selected pre-merger interacting galaxies are not strongly different from those of normal spirals. However, the $[8.0] - [24]$, $[3.6] - [24]$, and $[5.8] - [8.0]$ colors of the Arp galaxies are significantly redder on average than the spirals. This is consistent with previous IRAS studies, which showed that the IRAS $12\ \mu\text{m}$ to $25\ \mu\text{m}$ colors are redder in optically-selected pre-merger interacting galaxies than in normal spirals (Bushouse, Lamb, & Werner 1988; Surace,

Sanders, & Mazzarella 2004). Reddening of these colors is expected as the interstellar radiation field increases (Li & Draine 2001).

The $24\ \mu\text{m}$ band is the most sensitive of our filters to the SFR, as it is dominated by emission from very small grains, which are heated by the ultraviolet radiation field. In contrast, the $8\ \mu\text{m}$ band contains the dust emission features commonly attributed to polycyclic aromatic hydrocarbons (PAHs); these PAHs may be heated by the general interstellar radiation field. For star forming clumps in M51, Calzetti et al. (2005) found a direct proportionality between $24\ \mu\text{m}$ and extinction-corrected Paschen- α flux. In contrast, the $8\ \mu\text{m}/\text{Pa}\alpha$ ratio for these M51 clumps increases with decreasing luminosity, implying some PAH heating by non-ionizing photons. Thus to find weak enhancements in SFR, colors involving $24\ \mu\text{m}$ are best. The $[3.6] - [24]$ color is particularly valuable, as it is the cleanest measure of the ratio of the star formation rate to the total stellar mass.

The mean difference in $[3.6] - [24]$ color between the Arp disks and spirals is ~ 0.8 magnitudes. This corresponds to a mean enhancement in normalized SFR of 2.1 in the Arp disks. This is consistent with previous $\text{H}\alpha$ and far-infrared studies of optically-selected interacting systems (Bushouse 1987; Bushouse, Lamb, & Werner 1988; Kennicutt et al. 1987). As with these previous studies, there is a lot of scatter in this relation, with some Arp galaxies having little star formation enhancement. Starbursts tend to be physically localized within interacting galaxies, and have relatively short timescales compared to the timescale of the interaction. Thus they may not dominate the global stellar population over the duration of the interaction. An optically-selected sample of galaxies like our sample would have a range of interaction parameters and timescales, thus would tend to catch a lot of systems in a non-dominating-burst stage. For a strong burst to happen before a merger and to dominate the global infrared colors of the galaxy, the interaction parameters and timescale would have to be optimal. It is also possible that some of our spiral galaxies may not be completely isolated: they may be the result of recent minor mergers or interactions with distant or small companions, so our set of spirals may not be a perfect control sample.

As with the Arp galaxies as a whole, we see redder [8.0] – [24], [3.6] – [24], and [5.8] – [8.0] colors for the M51-like galaxies in our sample compared to spirals, and therefore enhanced star formation. This is in agreement with the results of Laurikainen, Salo, & Aparicio (1998), who found bluer optical colors in the central regions of nine out of thirteen M51-like galaxies they studied. As with their study, our result is very tentative since we have a very small M51 sample size. We note that strongly enhanced star formation is present in localized regions within some of our M51-like galaxies. For examples, see our detailed studies on Arp 107 (Smith et al. 2005) and Arp 82 (Hancock et al. 2006).

Examining the mid-infrared properties of the tails and bridges in our galaxies has been challenging because of the low level of mid-infrared emission from these regions. On average, the tidal features contribute less than 10% to the total Spitzer light from these galaxies. We cannot distinguish strong differences in the colors of the disks and tails, implying that the normalized SFR in the tails/bridges is probably similar to that in the disks, however, this is uncertain.

In most cases, we also cannot make any definitive conclusions about the colors of the non-spiral, non-Arp galaxy samples, because of our small sample size and the number of upper limits. We do, however, find significantly bluer [3.6] – [8.0] colors for the irregular/Sm galaxies than for the spirals. This is likely because of weakness in the mid-infrared PAH features, which contribute strongly to the 8 μm band. Weak PAH features and low 8 μm fluxes have been noted before in low metallicity systems (Madden 2000; Houck et al. 2004; Engelbracht et al. 2005; Dale et al. 2005; Madden et al. 2006; O’Halloran, Satyapal, & Dudik 2006).

The irregular/Sm galaxies also have slightly redder [3.6] – [4.5] colors than spirals, as previously found by Pahre et al. (2004). This may be due to younger stars on average (main sequence A stars are redder in this color than K giants; Reach et al. 2005) or higher interstellar-matter-to-stellar mass ratios; there may be larger fractional contributions from hot dust to the 4.5 μm band in irregular/Sm galaxies compared to spirals.

8.2. Spitzer and IRAS Luminosities vs. Absolute Star Formation Rates

Unlike the case with the observed distribution of Spitzer colors, KS tests cannot rule out that the observed distributions of 8.0 μm and 24 μm luminosities for the Arp disks and the spirals came from the same parent population. Since the fluxes in these bands can be used as a proxy for star formation (e.g., Förster Schreiber et al. 2004; Calzetti et al. 2005), this implies that the absolute rate of star formation in these Arp disks (as opposed to the mass-normalized rate) is similar to that in spirals. From their Pa α -24 μm correlation for star forming regions in M51, Calzetti et al. (2005) derived a relationship between the SFR (for 0.1 – 100 M_{\odot} stars) and the 24 μm luminosity of $\text{SFR}(M_{\odot} \text{ yr}^{-1}) \approx 4 \times 10^{-43} L_{24}(\text{erg s}^{-1})$. Wu et al. (2005) obtained the same relationship using global Spitzer, radio continuum, and H α fluxes for a sample of non-dwarf infrared-selected galaxies from the Spitzer First Look Survey. Combined with our median luminosities (Table 7), this relationship implies a median SFR of $\sim 1.7 M_{\odot} \text{ yr}^{-1}$ for our Arp galaxies, and $0.9 M_{\odot} \text{ yr}^{-1}$ for the spirals. The possibly lower implied masses for the Arp galaxies compared to the spirals (Section 4), combined with the relatively small sample sizes, may account for the lack of a significant difference in the distribution of luminosities.

For dusty starburst galaxies, another measure of the star formation rate can be obtained from the total 8 – 1000 μm infrared luminosity using the relationship in Kennicutt (1998). This gives, on average, a SFR of $\sim 2.6 M_{\odot} \text{ yr}^{-1}$ per disk in our Arp galaxies, and $\sim 0.9 M_{\odot} \text{ yr}^{-1}$ in the spirals. These are similar to the values obtained using the 24 μm luminosities. As noted by Kennicutt (1998) and many others (e.g., Persson & Helou 1987; Smith et al. 1991, 1994; Sauvage & Thuan 1992), in normal galaxies dust heating by non-OB stars can contribute to the far-infrared luminosity, thus the use of the Kennicutt relationship for non-starbursts may over-estimate the SFR in some cases. Calzetti et al. (2005) found that for the M51 clumps, Pa α scales directly with L_{24} but not with total far-infrared luminosity; there is an excess of far-infrared emission at low luminosities, implying heating by non-OB stars. If the fraction of dust heated by young stars contributing to the FIR emission varies from galaxy to galaxy, then

the L_{FIR}/SFR relationship may be different in interacting galaxies than in spirals. For example, in interacting galaxies the star formation is more centrally concentrated (see Section 7), perhaps due to gas being driven into the inner regions of the galaxy by the interaction. The dust associated with this central gas may be in closer proximity to both OB and non-OB stars, on average, than in normal spirals, producing a higher FIR luminosity for the same absolute star formation rate. In spite of these possible problems, however, the median SFRs that we obtain for the two samples from L_{24} and L_{IR} are similar.

To further investigate the question of SFR indicators and whether the conversion from L_{FIR} to SFR differs from galaxy to galaxy and between samples, in Figure 36 we provide histograms of $L_{24\mu m}/L_{FIR}$ for the Arp galaxies, the spirals, the M51-like galaxies, the Irr/Sm galaxies, and the Elliptical/S0 galaxies. For the Arp systems, the total flux of both galaxies in the pairs is included. For comparison, in Figure 37 we show the same histograms, but using the total 8 – 1000 μm infrared luminosity L_{IR} . For both the $L_{24\mu m}/L_{FIR}$ and $L_{24\mu m}/L_{IR}$ ratios, KS tests cannot rule out that the Arp and spiral samples originated from the same parent distribution. There is a spread in these two ratios from galaxy to galaxy, with a total range in the $L_{24\mu m}/L_{FIR}$ ratio of a factor of ~ 6 for the Arp galaxies. The spread in the L_{24}/L_{IR} ratio is slightly larger, with a total range of a factor of ~ 10 for the Arp galaxies. Note that L_{24} and L_{IR} are not completely independent, in that L_{IR} includes the 25 μm IRAS flux, thus an excess in L_{24} compared to L_{FIR} increases L_{IR} . Since the ratio of the star formation rates derived by the two methods, $\text{SFR}(24\ \mu m)/\text{SFR}(\text{IR})$, is simply proportional to L_{24}/L_{IR} , then the derived SFR for an individual galaxy can differ by up to a factor of ~ 10 , depending upon the method used. As our galaxies do not have strongly enhanced SFRs vs. normal spirals, the 24 μm luminosity may be a better tracer of star formation than the far-infrared. This is supported by models of the infrared spectral energy distribution in normal spirals, which suggest that the 20 – 42 μm range is the best tracer of star formation in normal star forming galaxies (Dale et al. 2001). Follow-up studies with bigger samples would be helpful in further investigating this issue.

8.3. Star Formation Enhancement vs. Pair Separation

No strong correlation between the Spitzer mid-infrared colors of the interacting systems and the projected pair separation is visible in our sample. A number of different factors likely contribute to weakening such a correlation. First, some scatter is introduced by the fact that we have only projected separations. Second, scatter is introduced because the strength of tidal star formation triggering during an interaction depends upon many other parameters in addition to separation and mass ratio, such as orbital parameters and interstellar gas content and distribution. Third, the observed projected separation is a complicated function of the orbital parameters and the timescale of the interaction, which differ from system to system. Some of our wider pairs may have already passed the point of closest approach and may be in the process of separating, thus may be in a burst phase. Numerical modeling shows that when a flyby encounter triggers a starburst, the burst often happens after the time of closest approach (e.g., Mihos, Richstone, & Bothun 1992).

In contrast to our Spitzer results, previous optical studies do measure a detectable difference in SFR between close pairs and wider pairs, though with a lot of scatter in the relationship (Barton et al. 2000; Lambas et al. 2003; Nikolic, Cullen, & Alexander 2004). Our lack of a detectable difference is likely due in part to a selection effect; our pairs were selected based on tidal distortion, while these other studies selected pairs based solely on proximity. Among our wider pairs, we probably include a higher fraction that are post-closest encounter. Another likely factor is our relatively small sample size. In the histograms of the $[8] - [24]$ and $[3.6] - [24]$ colors of the wide vs. close pairs (Figures 33 and 34), the reddest galaxies are in close pairs. However, this result is not statistically significant (Table 9). With a larger sample size, a significant difference may be discernable.

We note that the so-called ultra-luminous infrared galaxies (ULIRGs) (infrared-selected galaxies which have very high SFRs) tend to be either mergers or very close pairs (separation < 2 kpc) (Veilleux, Kim, & Sanders 2002). Our pairs have much larger separations, and so are in an earlier pre-merger state.

8.4. The Central Concentration of Star Formation

We have found that the $24\ \mu\text{m}$ distributions in the Arp disks are more centrally-concentrated than those of normal spirals. This implies that, even before merger, interactions can modify the radial distribution of the active star formation regions, by driving gas into the central region and triggering nuclear and circumnuclear star formation. This result is consistent with previous optical, near-infrared, radio continuum, and ground-based mid-infrared studies, which also implied enhanced central star formation in interacting galaxies (Joseph et al. 1984; Lonsdale, Persson, & Matthews 1984; Keel et al. 1985; Hummel et al. 1990; Barton Gillespie, Geller, & Kenyon 2003; Bergvall, Laurikainen, & Aalto 2003; Nikolic, Cullen, & Alexander 2004). Our observations show that, even in relatively low-luminosity pre-mergers, where the total L_{FIR} of a typical system is less than that of a so-called luminous infrared galaxy (i.e., $< 10^{11} L_{\odot}$), the effects of the tidal processes has already begun to operate on the disks, stimulating more activity in the center of the disk. These results are consistent with numerical models of gas buildup in the central regions of interacting galaxies, via bar- or wave-induced angular momentum transport, mass transfer between galaxies, and ring-like compression (e.g., Noguchi 1988; Barnes & Hernquist 1996; Struck & Smith 2003; Iono, Yun, & Mihos 2004). Such activity may be a prelude to dramatically increased nuclear activity when the galaxies fully merge.

9. Summary

We compare the Spitzer infrared luminosities and colors for a sample of 35 strongly interacting Arp galaxy pairs with those of 26 isolated spirals. The $[3.6] - [24]$, $[8.0] - [24]$, and $[5.8] - [8.0]$ colors of the Arp disks are significantly redder than those of the spirals. The $[3.6] - [24]$ colors of the Arp disks are 0.8 magnitudes redder, on average, than the spirals, implying an enhancement to the mass-normalized SFR of a factor of ~ 2 . For the shorter wavelength Spitzer colors ($[3.6] - [4.5]$, $[4.5] - [5.8]$, and $[3.6] - [8.0]$) we cannot detect a significant difference between spirals and Arp galaxies. This is likely because these bands are less sensitive to star formation, and include a larger fraction of

emission not related to star formation.

We see little statistical difference in the $3.6\ \mu\text{m}$, $8.0\ \mu\text{m}$, and $24\ \mu\text{m}$ luminosities of the Arp and spiral samples. However, some of the small Arp companions have low $3.6\ \mu\text{m}$ luminosities, and therefore low masses, compared to spirals. The Spitzer colors are more sensitive to small interaction-induced enhancements in star formation rate than the Spitzer luminosities, because they are normalized for mass. The Arp disks have more centrally-concentrated $24\ \mu\text{m}$ emission than the normal spirals, implying that the interactions have driven gas into the central regions, triggering central star formation. No trend of Spitzer colors with pair separation is visible in our sample. This may be a selection effect, as our galaxies were chosen to have strong tidal distortions.

We thank the Spitzer team for making this research possible. We also thank Rob Kennicutt and the SINGS team for producing the SINGS dataset. We thank Edith Seier and Mark Giroux for helpful communications and Amanda Moffett for help with the analysis. This research was supported by NASA Spitzer grant 1263924, NSF grant AST-0097616, and NASA LTSA grant NAG5-13079. This research has made use of the NASA/IPAC Extragalactic Database (NED) which is operated by the Jet Propulsion Laboratory, California Institute of Technology, under contract with the National Aeronautics and Space Administration.

REFERENCES

- Allamandola, L. J., Tielens, A. G. G. M., & Barker, J. R. 1985, *ApJ*, 290, L25
- Arp, H. 1966, *Atlas of Peculiar Galaxies* (Pasadena: Caltech)
- Barnes, J. E., & Hernquist, L. 1996, *ApJ*, 471, 115
- Barton, E. J., Geller, M. J., & Kenyon, S. J. 2000, *ApJ*, 530, 660
- Barton Gillespie, E., Geller, M. J., & Kenyon, S. J. 2003, *ApJ*, 582, 668
- Bergvall, N., Laurikainen, E. & Aalto, S. (2003), *A&A* 405, 31
- Bloemen, J. B. G. M., et al. 1986, *A&A*, 154, 25

- Boselli, A., Lequeux, J., & Gavazzi, G. 2004, *A&A*, 428, 409
- Bundy, K., Fukugita, M., Ellis, R. S., Kodama, T., & Conselice, C. J. 2004, *ApJ*, 601, L123
- Charmandaris, V., Stacey, G.J., & Gull, G. 2002, *ApJ*571, 282.
- Bushouse, H. A. 1987, *ApJ*, 320, 49
- Bushouse, H. A., Lamb, S. A., & Werner, M. W. 1988, *ApJ*, 335, 74
- Calzetti, D., et al. 2005, *ApJ*, 633, 871
- Dahari, O. 1985, *ApJS*, 57, 643
- Dale, D. A., Helou, G., Contursi, A., Silbermann, N. A., & Kolhatkar, S. 2001, *ApJ*, 549, 215
- Dale, D. A., et al. 2005, *ApJ*, 633, 857
- Elmegreen, D. M., Elmegreen, B. G., Kaufman, M., Sheth, K., Struck, C., Thomasson, M., & Brinks, E. 2006, *ApJ*, 642, 158
- Engelbracht, C. W., Gordon, K. D., Rieke, G. H., Werner, M. W., Dale, D. A., & Latter, W. B. 2005, *ApJ*, 628, 23
- Fazio, G. G., et al. 2004, *ApJS*, 154, 10
- Förster Schreiber, N. M., Roussel, H., Sauvage, M., & Charmandaris, V. 2004, *A&A*, 419, 501
- Hatziminaoglou, E., et al. 2005, *AJ*, 129, 1198
- Hancock, M., Smith, B. J., Struck, C., Giroux, M. L., Appleton, P. N., Charmandaris, V., & Reach, W. T. 2006, *AJ*, submitted
- Heckman, T. M., Robert, C., Leitherer, C., Garnett, D. R., & van der Rydt, F. 1998, *ApJ*, 503, 646
- Helou, G., Malhotra, S., Hollenbach, D. J., Dale, D. A., & Contursi, A. 2001, *ApJ*, 548, L73
- Hollenbach, D. J., & Tielens, A. G. G. M. 1997, *ARA&A*, 35, 179
- Houck, J. R., et al. 2004, *ApJS*, 154, 211
- Hummel, E., van der Hulst, J. M., Kennicutt, R. C. & Keel, W. C. 1990, *A&A*, 236, 333
- Iono, D., Yun, M. S., & Mihos, J. C. 2004, *ApJ*, 616, 199
- Joseph, R. D., Meikle, W. P. S., Robertson, N. A., & Wright, G. S. 1984, *MNRAS*, 209, 111
- Keel, W. C., Kennicutt, R. C., Jr., Hummel, E., & van der Hulst, J. M. 1985, *AJ*, 90, 708
- Kim, D.-C., Sanders, D. B., Veilleux, S., Mazzarella, J. M., & Soifer, B. T. 1995, *ApJS*, 98, 129
- Kennicutt, R. C., Jr. 1998, *ApJ*, 498, 541
- Kennicutt, R. C., Jr., et al. 2003, *PASP*, 115, 928
- Kennicutt, R. C., Jr., Keel, W. C., van der Hulst, J. M., Hummel, E., & Roettiger, K. A. 1987, *AJ*, 93, 1011
- Lambas, D. G., Tissera, P. B., Alonso, M. S., & Coldwell, G. 2003, *MNRAS*, 346, 1189
- Larson, R. B. & Tinsley, B. M. 1978, *ApJ*, 219, 46
- Laurikainen, E., Salo, H., & Aparicio, A. 1998, *A&A*, 129, 517
- Léger, A., & Puget, J. L. 1984, *A&A* 137, L5
- Le Fèvre, O., et al. 2000, *MNRAS*, 311, 565
- Metcalfe, L., et al. 2005, *A&A*, 444, 777
- Li, A. & Draine, B. T. 2001, *ApJ*, 554, 778
- Li, A. & Draine, B. T. 2002, *ApJ*, 572, 232
- Lonsdale, C. J., Persson, S. E., & Matthews, K. 1984, *ApJ*, 287, 95
- Lonsdale, C. J., Helou, G., Good, J. C., & Rice, W. 1985, *Cataloged Galaxies and Quasars Observed in the IRAS Survey, Version 1, Appendix B*.
- Nikolic, B., Cullen, H., & Alexander, P. 2004, *MNRAS*, 355, 874
- Madden, S. C. 2000, *NewAR*, 44, 249
- Madden, S. C., Galliano, F., Jones, A. P., & Sauvage, M. 2006, *A&A*, 446, 877
- Mihos, J. C., Richstone, D. O., & Bothun, G. D. 1992, *ApJ*, 400, 153

- Mirabel, I. F., et al. 1991, *A&A*, 243, 367
- Mirabel, I. F., et al. 1992, *A&A*, 256, L19
- Morris, S. L., & van den Bergh, S. 1994, *ApJ*, 427, 696
- Moshir, M., et al. 1992, Explanatory Supplement to the IRAS Faint Source Catalog, Version 2 (JPL D-10015) (Pasadena: JPL)
- Noguchi, M. 1988, *A&A*, 203, 259
- O’Halloran, B., Satyapal, S., & Dudik, R. P. 2006, *ApJ*, 641, 795
- Pahre, M. A., Ashby, M. L. N., Fazio, G. G., & Willner, S. P. 2004, *ApJS*, 154, 235
- Perault, M. 1987, Ph.D. Dissertation, University of Paris
- Persson, C. J. L., & Helou, G. 1987, *ApJ*, 314, 513
- Reach, W. T. et al. 2005, *PASP*, 117, 978
- Rieke, G. H., et al. 2004, *ApJS*, 154, 25
- Roussel, H., Sauvage, M., Vigroux, L., & Bosma, A. 2001, *A&A*, 372, 427
- Roussel, H., et al. 2006, *ApJ*, 646, 841
- Sauvage, M. & Thuan, T. T. 1992, *ApJ*, 396, L69
- Sanders, D. B. & Mirabel, I. F. 1996, *ARA&A*, 34, 749
- Sanders, D. B., Mazzarella, J. M., Kim, D.-C., Surace, J. A., & Soifer, B. T. 2003, *AJ*, 126, 1607
- Sanders, D. B., Soifer, B. T., Elias, J. H., Madore, B. F., Matthews, K., Neugebauer, G., & Scoville, N. Z. 1988, *ApJ*, 325, 74
- Schechter, P. 1980, *AJ*, 85, 801
- Schombert, J. M., Wallin, J. F., & Struck-Marcell, C. 1990, *AJ*, 99, 497
- Schweizer, F. 1978, in *Structure and Properties of Nearby Galaxies*, ed. E. M. Berkhuijsen & R. Wielebinski (Dordrecht: Reidel), 279
- Smith, B. J., Harvey, P. M., Colomé, C., Zhang, C. Y., DiFrancesco, J., & Pogge, R. W. 1994, *ApJ*, 425, 91
- Smith, B. J., Lester, D. F., Harvey, P. M., & Pogge, R. W. 1991, *ApJ*, 380, 677
- Smith, B. J., Kleinmann, S. G., Huchra, J. P., & Low, F. 1987, *ApJ*, 318, 161
- Smith, B. J., Struck, C., Appleton, P. N., Charmandaris, V., Reach, W., & Eitter, J. J. 2005, *AJ*, 130, 2117
- Smith, B. J., Struck, C., & Pogge, R. W. 1997, *ApJ*, 483, 754
- Soifer, B. T., Sanders, D. B., Madore, B. F., Neugebauer, G., Danielson, G. E., Elias, J. H., Lonsdale, C. J., & Rice, W. L. 1987, *ApJ*, 320, 238
- Struck-Marcell, C., & Tinsley, B. M. 1978, *ApJ*, 221, 562
- Struck, C. 1999, *Phys. Rep.*, 321, 1
- Struck, C. & Smith, B. J. 2003, *ApJ*, 589, 157
- Surace, J. A., Sanders, D. B., & Mazzarella, J. M. 2004, *AJ*, 127, 3235
- Van den Bergh, S. 2000, *PASP*, 112, 529
- Veilleux, S., Kim, D.-C., & Sanders, D. B. 2002, *ApJS*, 143, 315
- Werner, M. W., et al. 2004, *ApJS*, 154, 1
- Whitney, B. A., et al. 2004, *ApJS*, 154, 315
- Wu, H., Cao, C., Hao, C.-N., Liu, F.-S., Wang, J.-L., Xia, X.-Y., Deng, Z.-G., & Young, C. K. 2005, *ApJ*, 632, L79

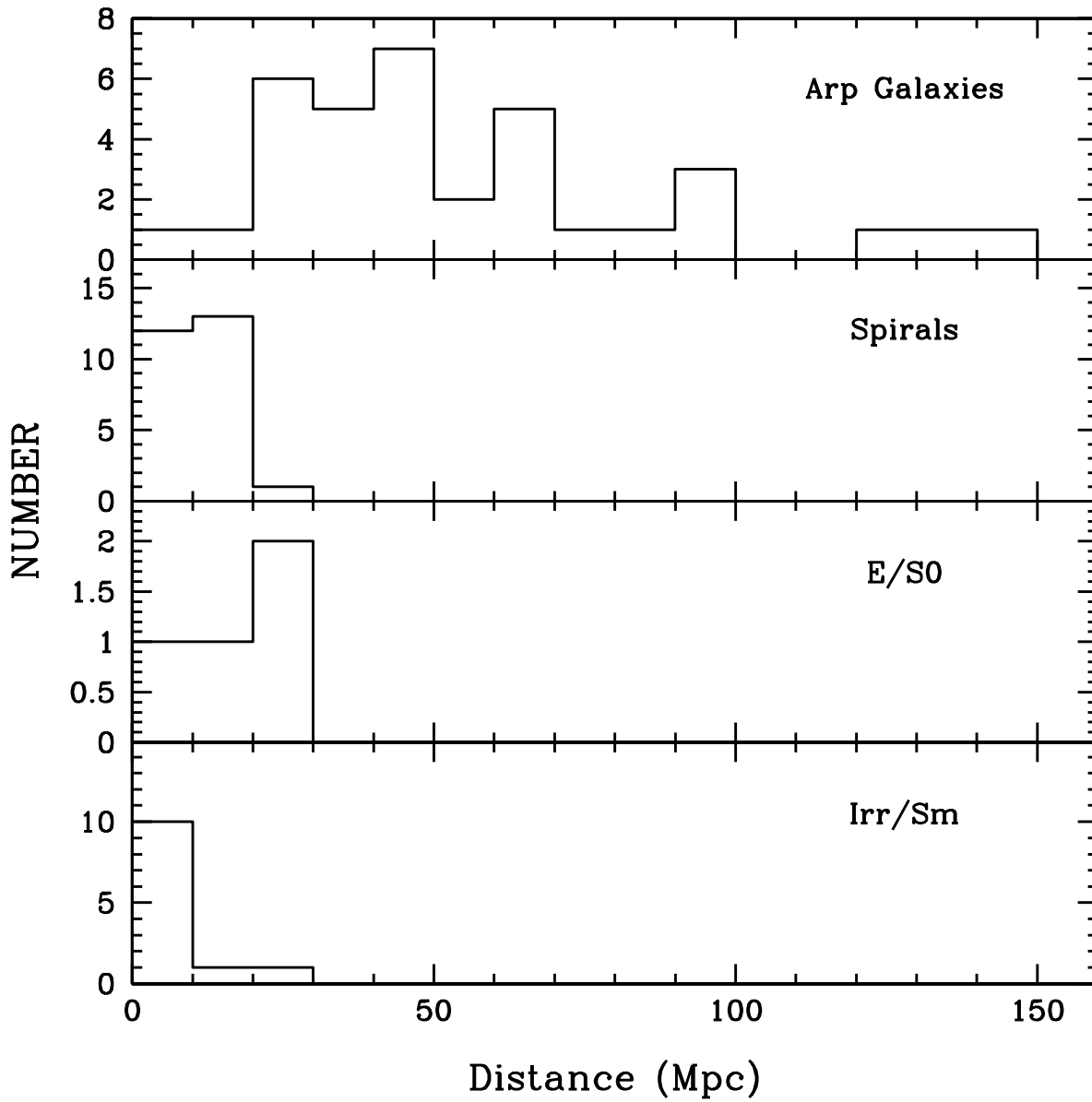


Fig. 1.— Histograms of the distances to the four samples of galaxies. Top panel: interacting sample. Middle panel: spiral sample. Third panel: Elliptical/S0 sample. Bottom panel: Irregular/Sm sample.

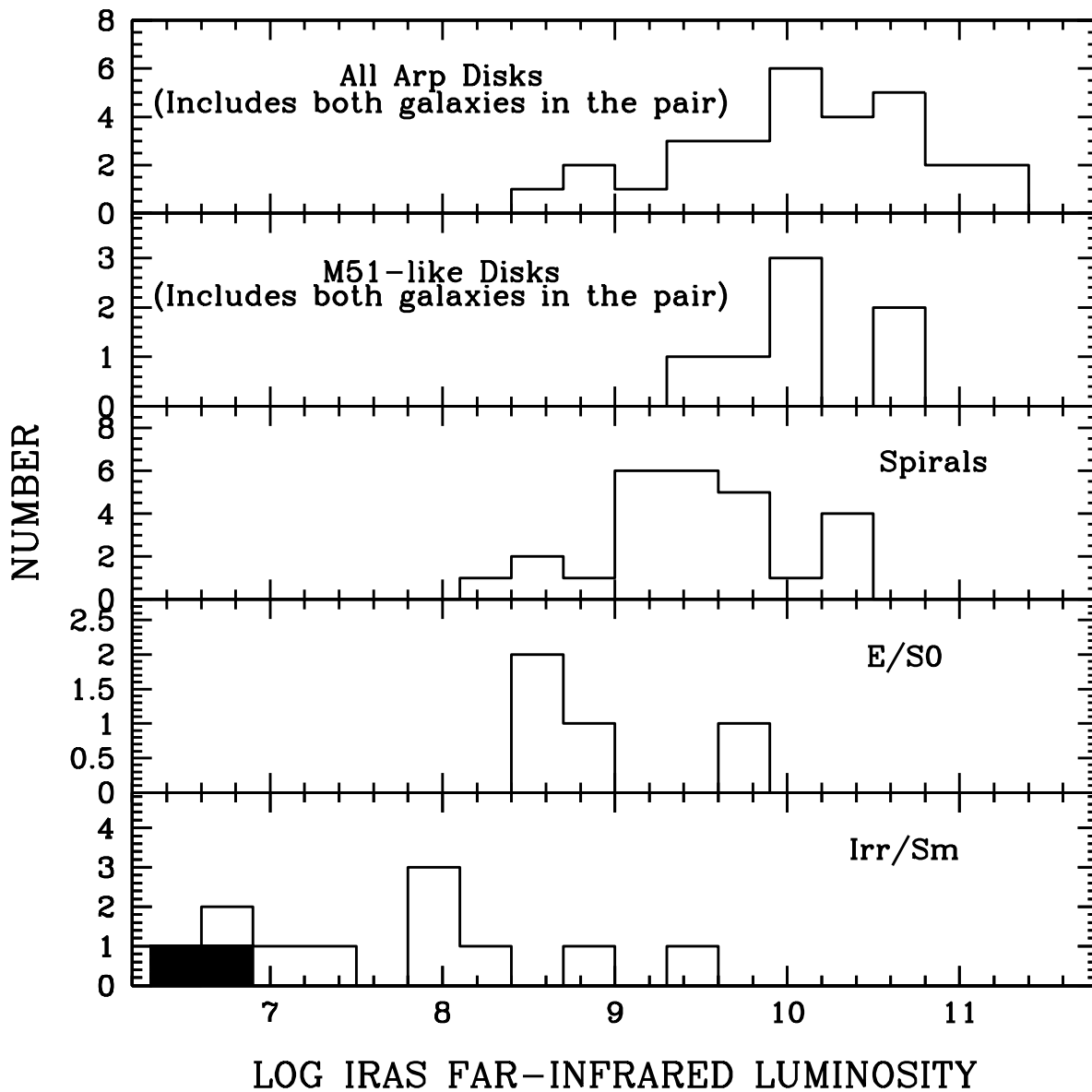


Fig. 2.— Histograms of the far-infrared luminosities of the various samples. Upper limits are indicated by shaded regions. Note that the luminosities for the Arp galaxies and M51-like galaxies include the combined flux from both galaxies in the pair. Top panel: interacting sample. Second panel: M51-like galaxies. Third panel: spiral sample. Fourth panel: Elliptical/S0 sample. Bottom panel: Irregular/Sm sample.

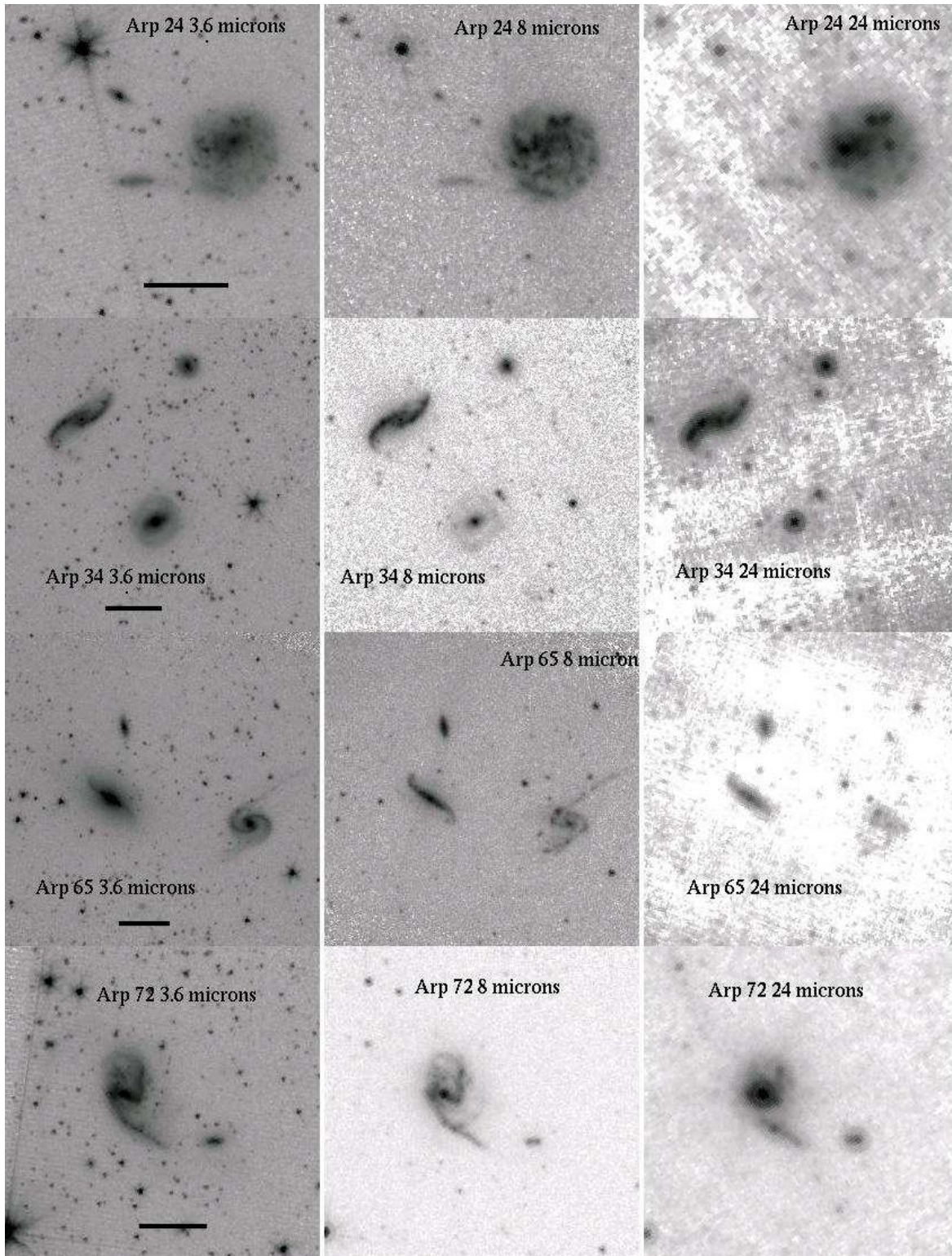


Fig. 3.— The 3.6 μm , 8.0 μm , and 24 μm images of galaxies in the interacting galaxy sample. North is up and east to the left. The scale bar is 60'' (1'). The 8 and 24 μm images are displayed with the same spatial scale as the 3.6 μm image. In Figures 3 – 11, the galaxies are plotted in order of Arp number. For identification of individual galaxies in the pairs, see Table 5. In the Arp 24 and 65 3.6 μm images, the small galaxies in the northeast (upper left) are background galaxies, so are not included in Table 5.

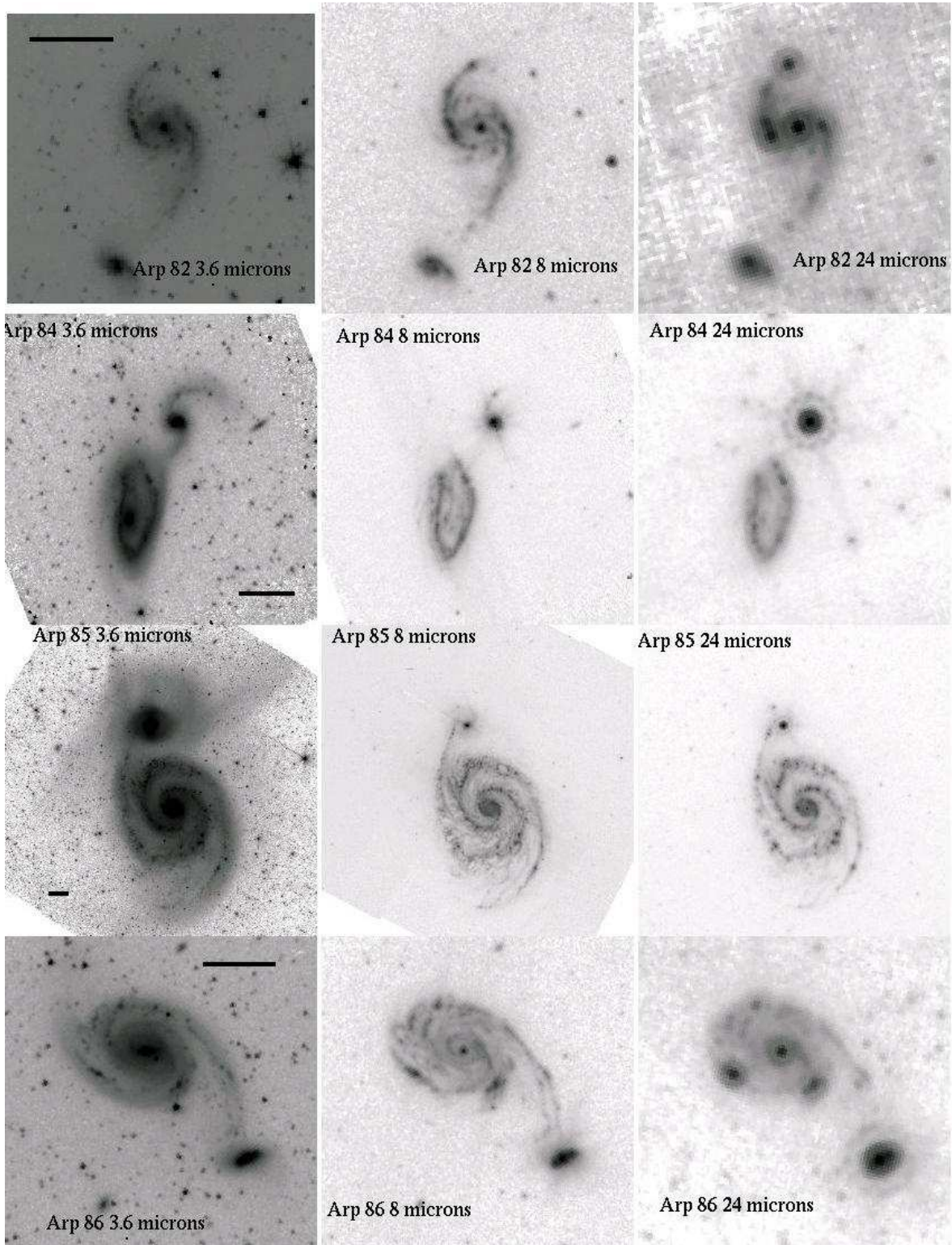


Fig. 4.— The 3.6 μm , 8.0 μm , and 24 μm images of galaxies in the interacting galaxy sample. North is up and east to the left. The scale bar is 60'' (1'). In the 24 μm Arp 84 image, the MIPS point spread function is visible as a 'ring' and 'spikes' around the very bright nucleus of the northern galaxy.

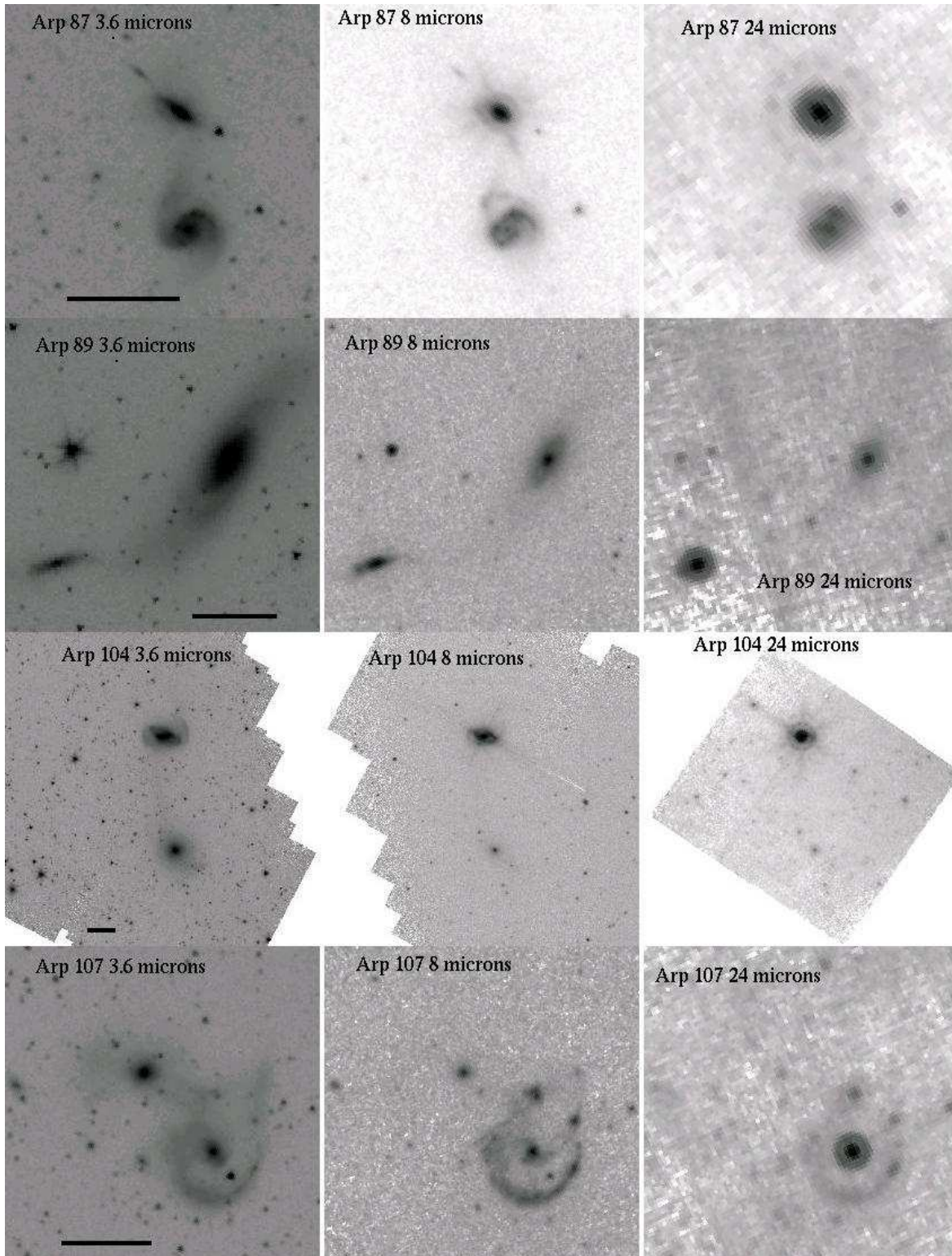


Fig. 5.— More the 3.6 μm , 8.0 μm , and 24 μm images of the sample galaxies. North is up and east to the left. The scale bar is 60'' (1'). No redshift is available for the small feature seen to the northeast of the northern galaxy in Arp 87, thus it is uncertain whether this is associated with the Arp pair or not. It is not included in the following statistics. In the 24 μm Arp 87 and Arp 104 images, the MIPS point spread function is visible around the very bright nuclei of the northern galaxies. The ring in Arp 107 is a real physical structure (see Smith et al. (2005) for a detailed study of the Spitzer Arp 107 images).

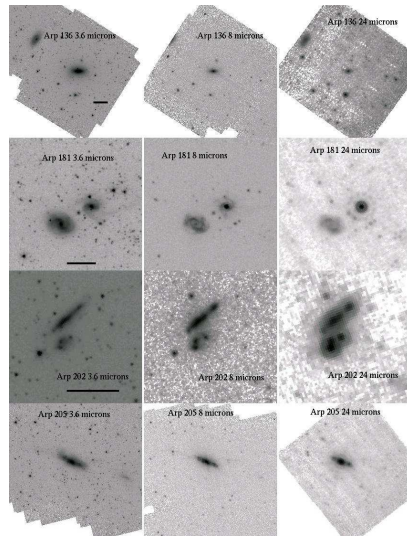


Fig. 6.— The $3.6 \mu\text{m}$, $8.0 \mu\text{m}$, and $24 \mu\text{m}$ images of galaxies in the interacting galaxy sample. North is up and east to the left. The scale bar is $60''$ ($1'$). In the Arp (1966) Atlas, Arp 136 consists of only NGC 5820, the large galaxy near the center of the images shown above. NGC 5820 has a similar-mass companion outside of the Arp Atlas field of view, NGC 5821. This second galaxy is visible in the northeast (upper left) of the images shown above. Unfortunately NGC 5821 was missed by our 4.5 and $8.0 \mu\text{m}$ Spitzer observations. The small galaxy to the south of NGC 5820 is a background galaxy. In the $24 \mu\text{m}$ Arp 181 image, the MIPS point spread function is visible as a ‘ring’ and ‘spikes’ around the very bright nucleus of the northern galaxy.

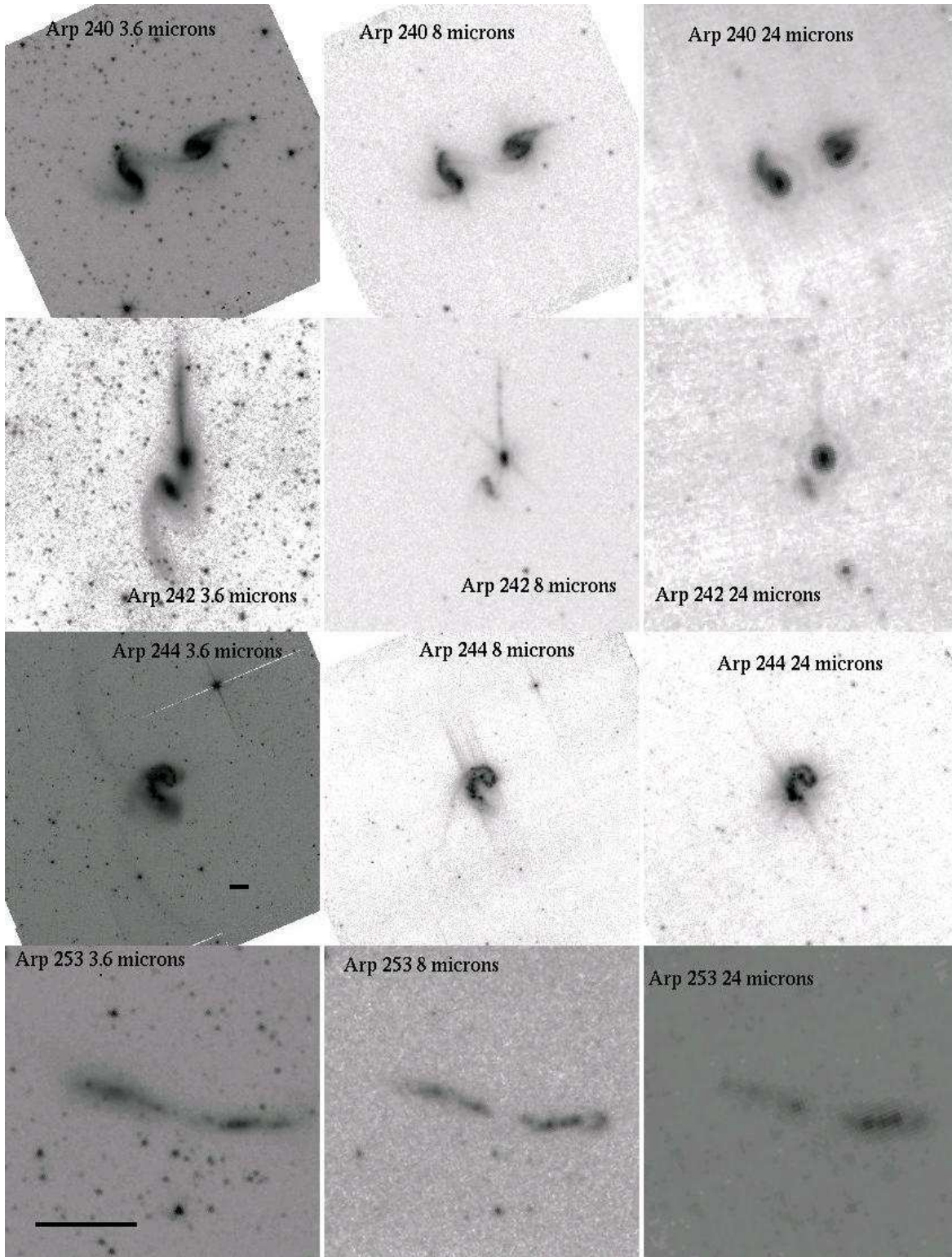


Fig. 7.— The $3.6\ \mu\text{m}$, $8.0\ \mu\text{m}$, and $24\ \mu\text{m}$ images of galaxies in the interacting galaxy sample. North is up and east to the left. The scale bar is $60''$ ($1'$). In the $24\ \mu\text{m}$ Arp 242 image, the MIPS point spread function is visible around the nucleus of the northern galaxy.

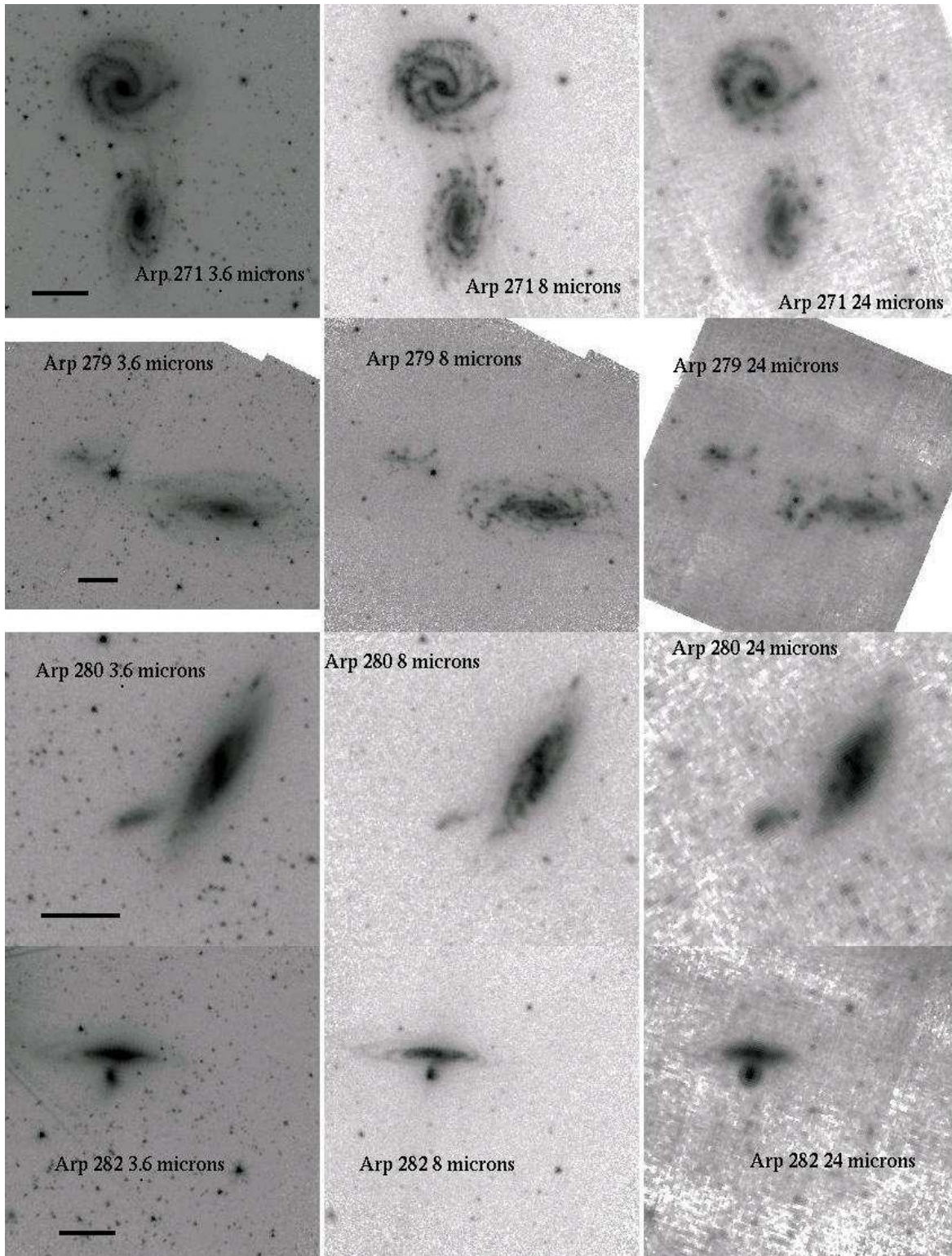


Fig. 8.— The 3.6 μm , 8.0 μm , and 24 μm images of galaxies in the interacting galaxy sample. North is up and east to the left. The scale bar is 60'' (1').

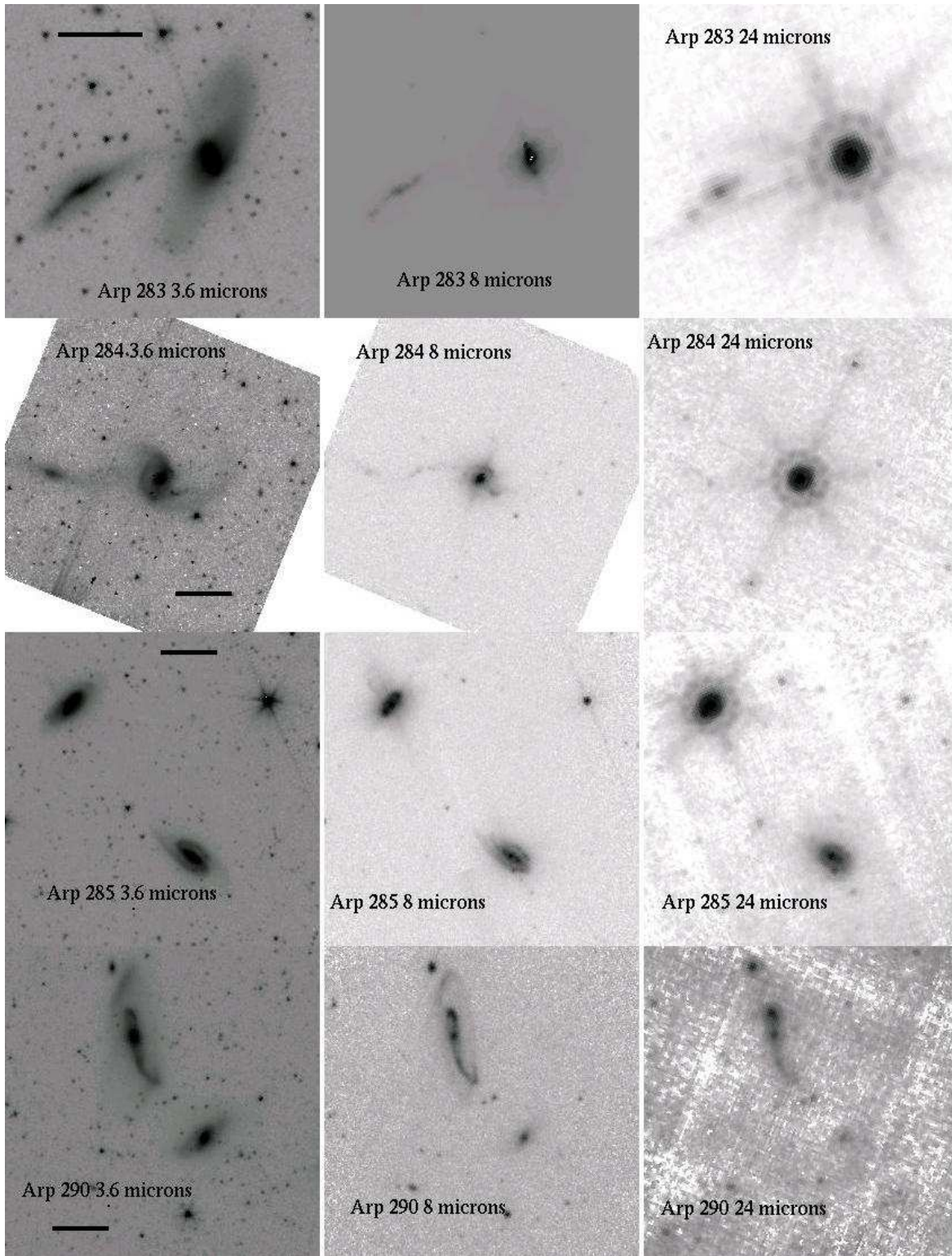


Fig. 9.— The 3.6 μm , 8.0 μm , and 24 μm images of galaxies in the interacting galaxy sample. North is up and east to the left. The scale bar is 60'' (1'). In the 24 μm Arp 283, Arp 284, and Arp 285 images, the MIPS point spread function is visible. The small object in the northeast (upper left) of the Arp 290 images is a background galaxy.

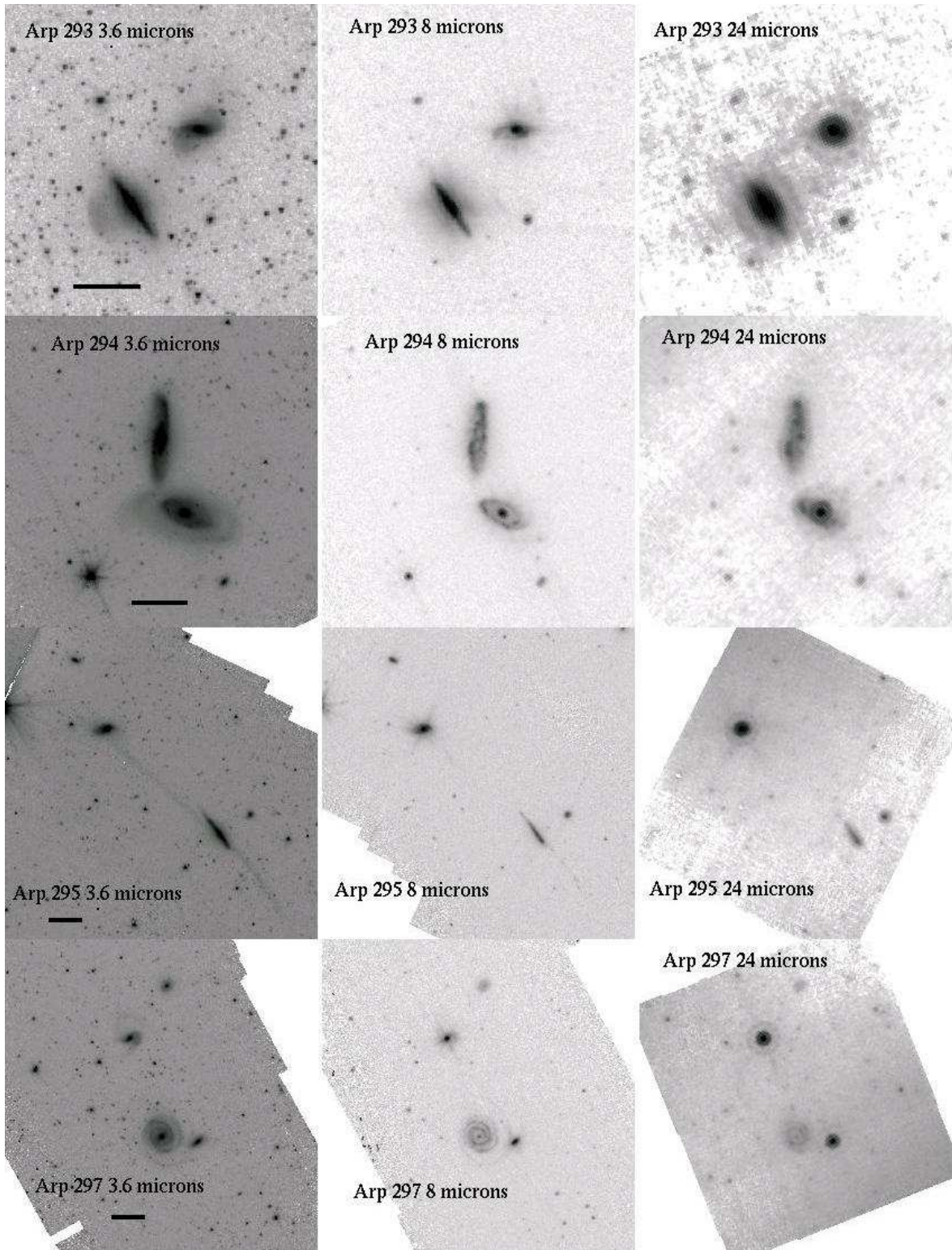


Fig. 10.— The 3.6 μm , 8.0 μm , and 24 μm images of galaxies in the interacting galaxy sample. North is up and east to the left. The scale bar is 60'' (1'). In the 24 μm Arp 295 and Arp 297 images, the MIPS point spread function is visible as a 'ring' and 'spikes' around the very bright nucleus of the northern galaxy.

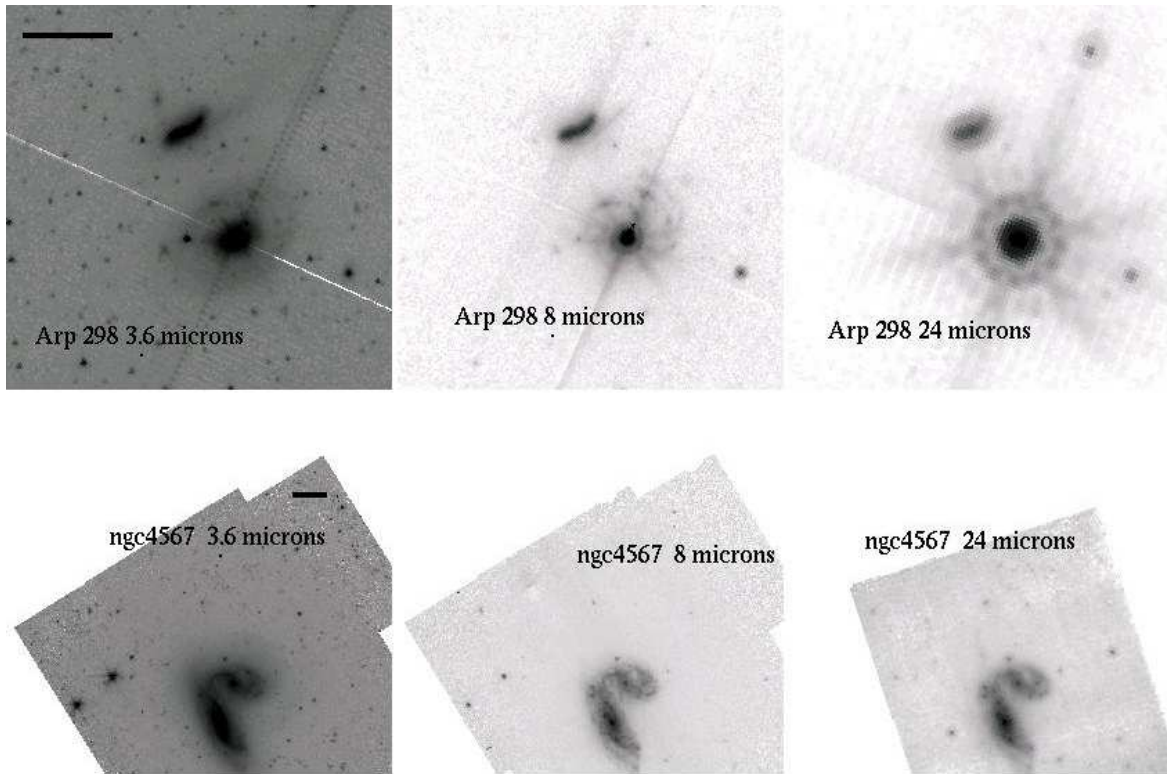


Fig. 11.— The 3.6 μm , 8.0 μm , and 24 μm images of galaxies in the interacting galaxy sample. North is up and east to the left. The scale bar is 60'' (1'). The MIPS PSF is visible in the 24 μm Arp 298 image.

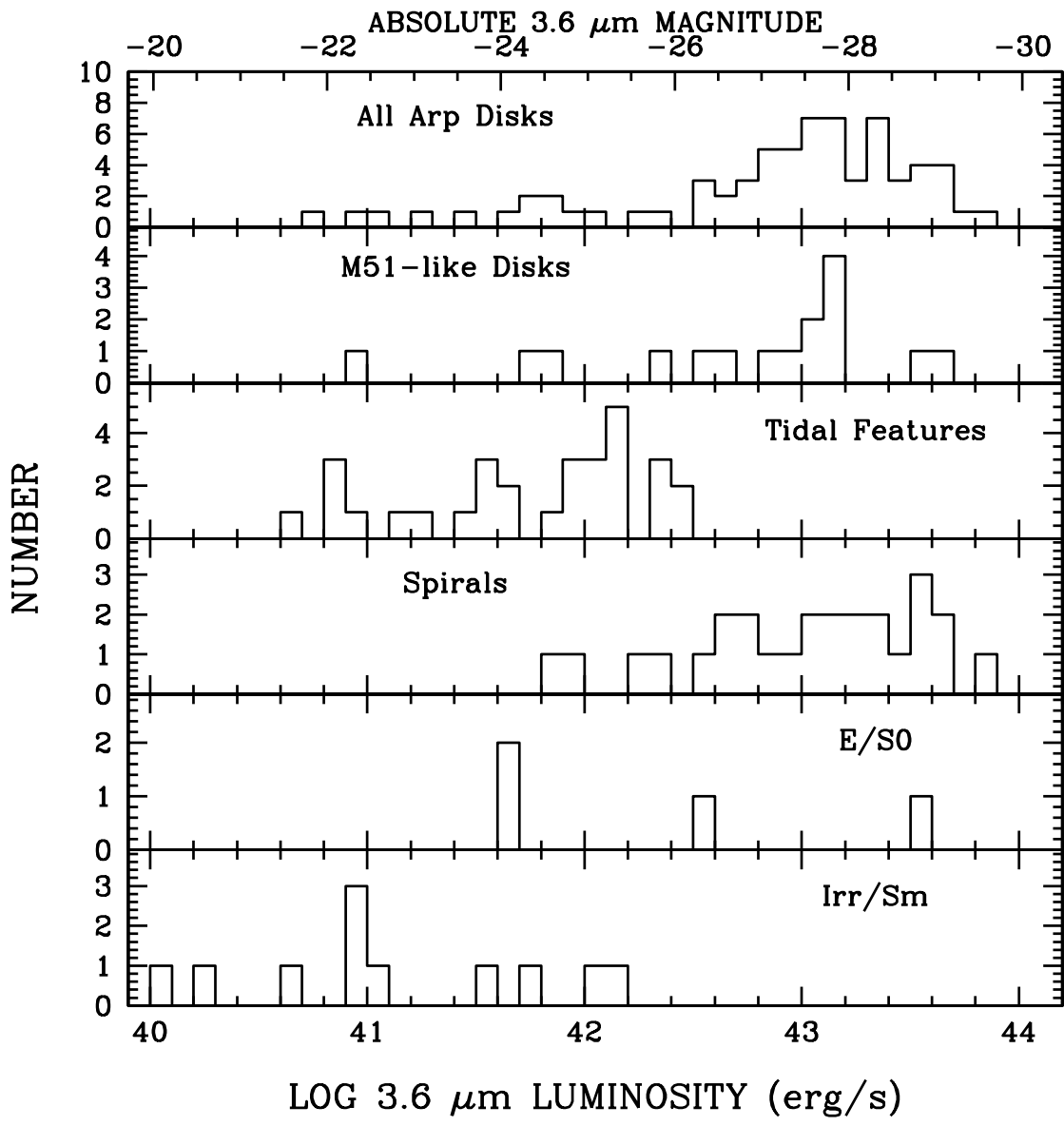


Fig. 12.— Histograms of the 3.6 μm luminosities for the various samples. For consistency with previous work (e.g., Calzetti et al. 2005), we use the ‘monochromatic’ luminosity νL_ν , using a frequency of 8.45×10^{13} Hz.

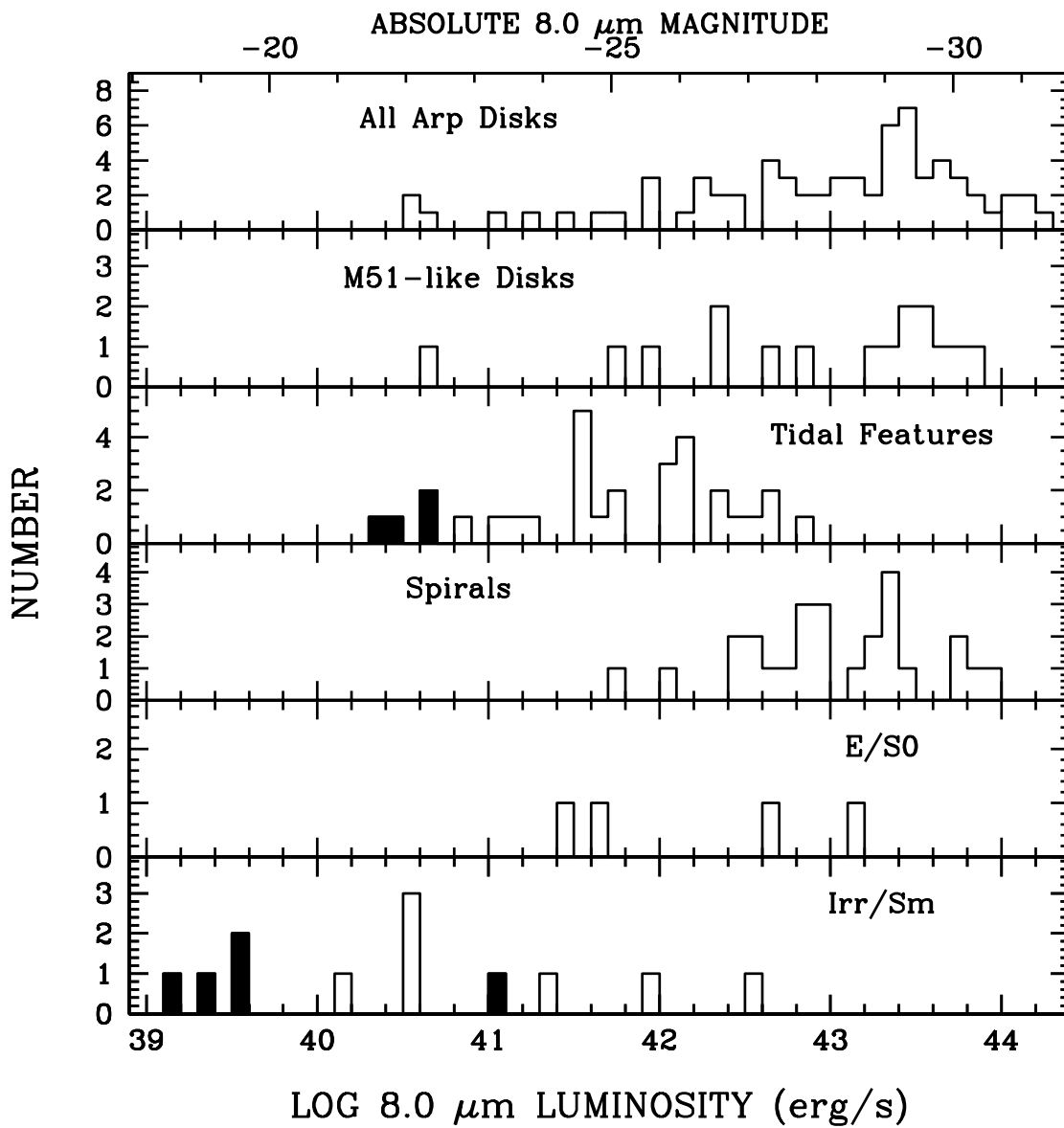


Fig. 13.— Histograms of the 8.0 μm luminosities for the various samples. For consistency with previous work, we use the ‘monochromatic’ luminosity νL_ν , using a frequency of 3.81×10^{13} Hz. Upper limits are indicated by shaded regions.

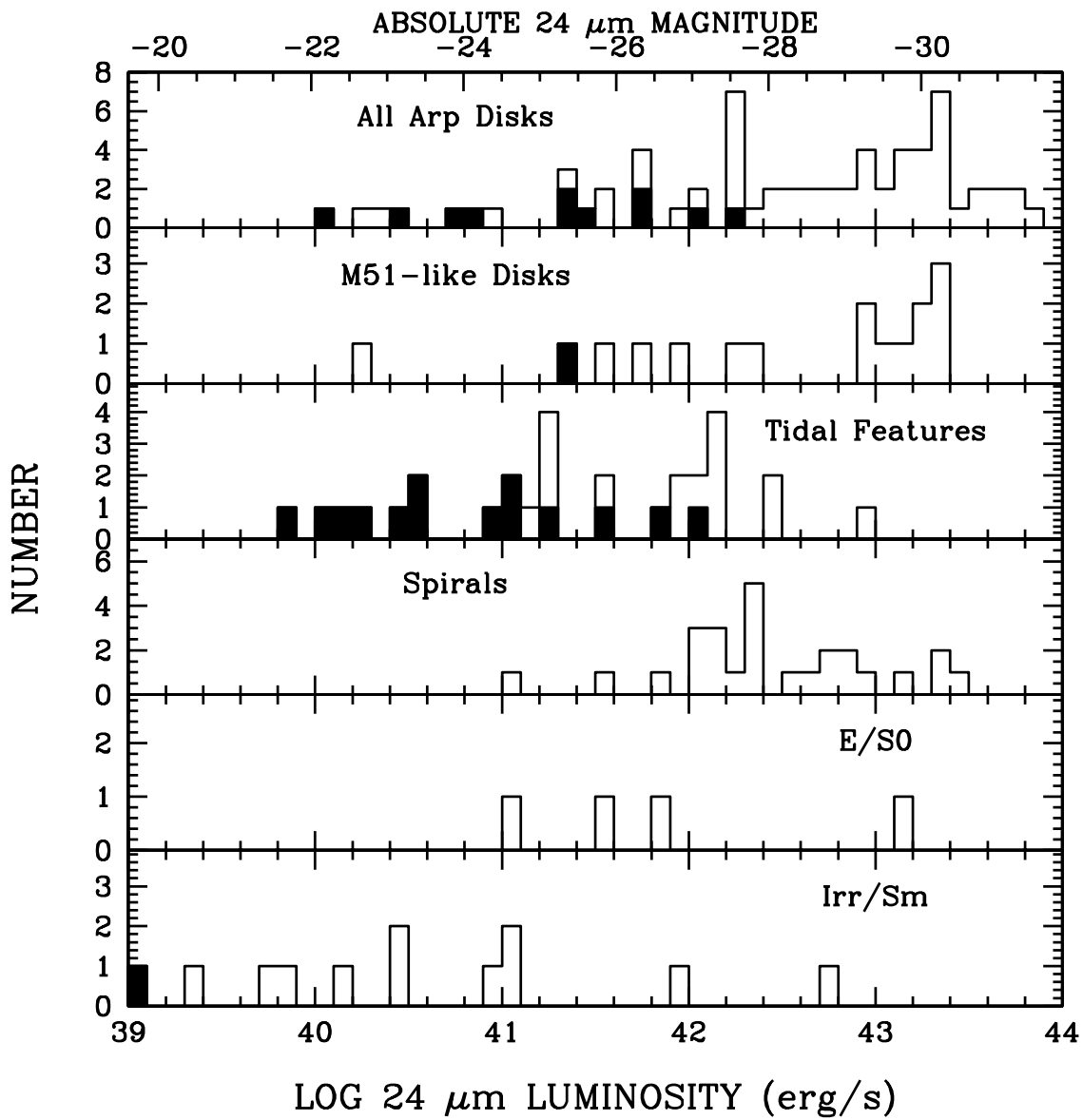


Fig. 14.— Histograms of the 24 μm luminosities for the various samples. For consistency with previous work, we use the ‘monochromatic’ luminosities νL_ν , using a frequency of 1.27×10^{13} Hz. The Arp galaxy with the highest luminosity is NGC 7469 (Arp 298), a Seyfert galaxy. Upper limits are indicated by the filled-in regions.

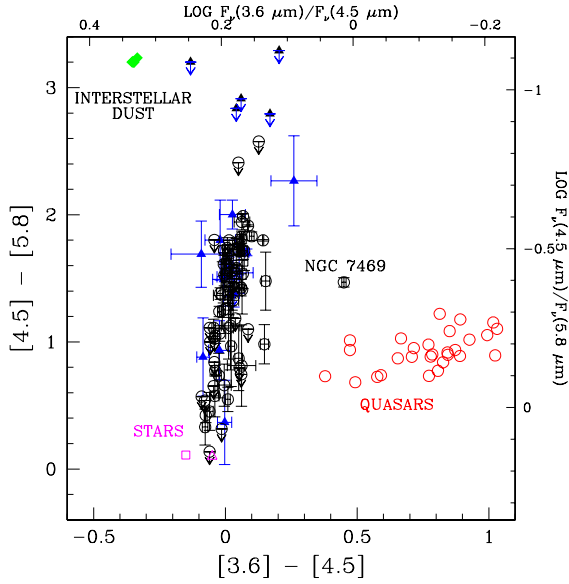


Fig. 15.— The Spitzer IRAC $[3.6] - [4.5]$ vs. $[4.5] - [5.8]$ color-color plot for the main disks of the interacting galaxy sample (black circles) and the tidal features of these galaxies (filled blue triangles). The colors of M0III stars (open magenta square), (M. Cohen 2005, private communication), and the mean colors of the field stars of Whitney et al. (2004) (magenta triangle), and the colors of the Hatziminaoglou et al. (2005) quasars (red circles) are also shown. The predicted IRAC colors for interstellar dust (Li & Draine 2001) are also plotted (filled green diamonds), for ISRF strengths that vary from $0.3 - 10,000 \times$ that in the solar neighborhood. As the ISRF increases, the IRAC colors of dust become redder. Note that the predicted dust colors vary very little for this wide range in ISRF. The Arp disk at $[3.6] - [4.5] = 0.4$ is the Seyfert galaxy NGC 7469.

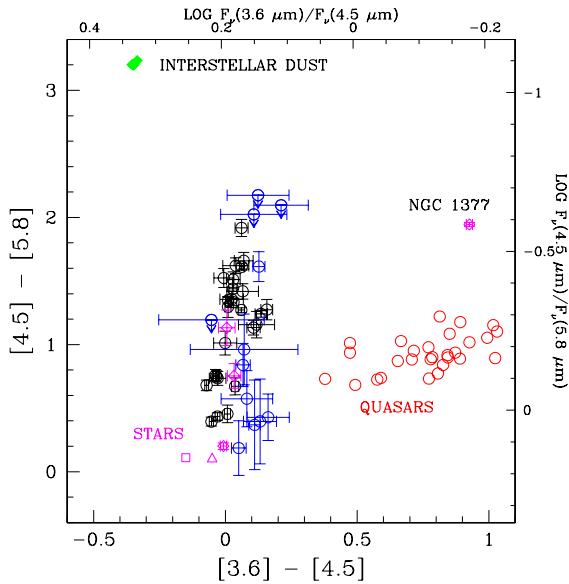


Fig. 16.— The Spitzer IRAC $[3.6] - [4.5]$ vs. $[4.5] - [5.8]$ color-color plot for the spiral galaxies (black circles), ellipticals/S0 (open magenta diamonds), and irregular/Sm galaxies (blue). The colors of M0III stars (open magenta square), field stars (magenta triangle), quasars (red circles), and interstellar dust (filled green diamonds) are also shown. The elliptical galaxy NGC 1377, like the Seyfert NGC 7469 (Figure 15), has a very red $[3.6] - [4.5]$ color, similar to that of quasars, in spite of not being classified as a Seyfert based on optical data (e.g., Kim et al. 1995). Our Spitzer fluxes for NGC 1377 are consistent with those of Dale et al. (2005). See Roussel et al. (2006) for a detailed discussion of NGC 1377. The bluest elliptical is NGC 4125.

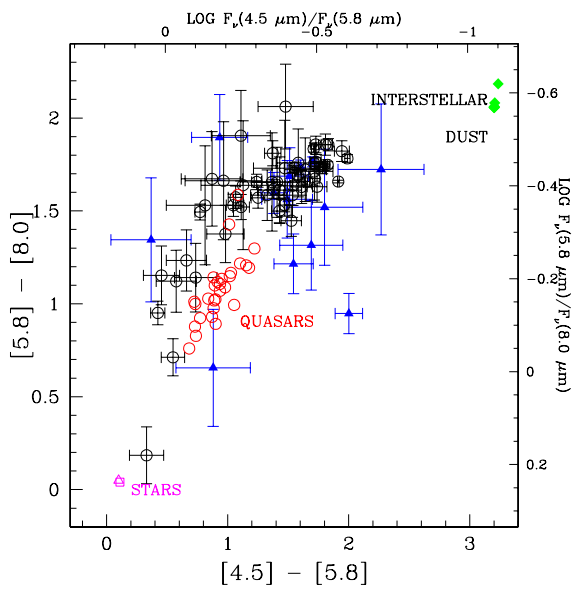


Fig. 17.— The Spitzer IRAC $[4.5] - [5.8]$ vs. $[5.8] - [8.0]$ color-color plot for the main disks of the interacting galaxy sample (black circles) and the tidal features of these galaxies (filled blue triangles). The colors of M0III stars (open magenta square), field stars (magenta triangle), quasars (red circles), and interstellar dust (filled green diamonds) are also shown. The bluest disk is Arp 290 south (IC 195).

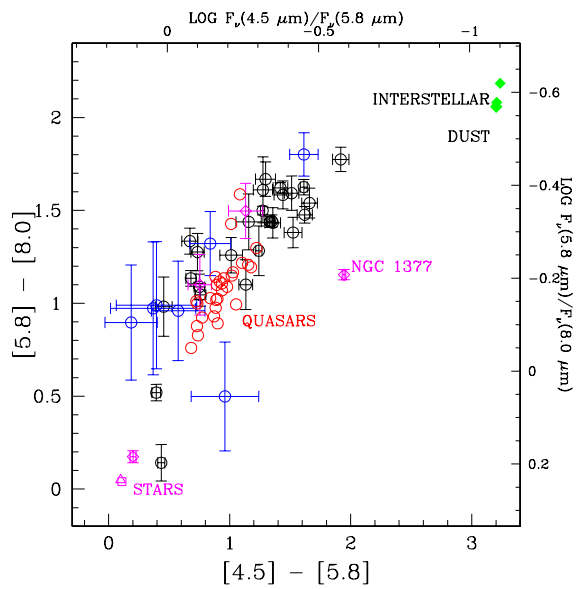


Fig. 18.— The Spitzer IRAC $[4.5] - [5.8]$ vs. $[5.8] - [8.0]$ color-color plot for the spiral galaxies (black circles), ellipticals/S0 (open magenta diamonds), and irregular/Sm galaxies (blue). The colors of M0III stars (open magenta square), field stars (magenta triangle), quasars (red circles), and interstellar dust (filled green diamonds) are also shown. The elliptical NGC 1377 again has peculiar colors. The bluest elliptical is NGC 4125.

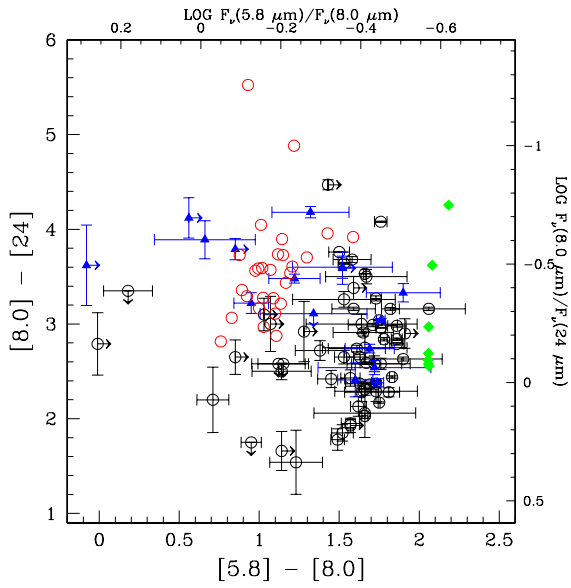


Fig. 19.— The Spitzer IRAC [5.8] – [8.0] vs. [8.0] – [24] color-color plot for the main disks of the interacting galaxy sample (black circles) and the tidal features of these galaxies (filled blue triangles). The colors of quasars (red circles) and interstellar dust (filled green diamonds) are also shown. Stellar photospheres are expected to lie at 0,0 on this plot. The tidal feature that is the reddest in [8.0] – [24] is the western tail of Arp 284 (NGC 7714/5), which has a bright star forming region near its base (see Smith, Struck, & Pogge 1997).

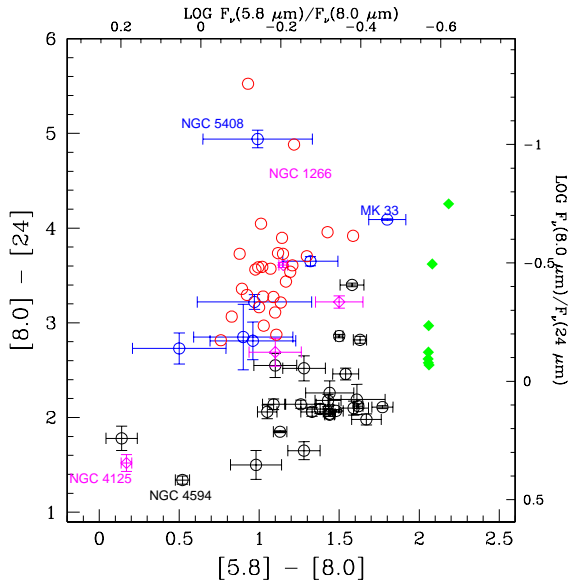


Fig. 20.— The Spitzer IRAC $[5.8] - [8.0]$ vs. $[8.0] - [24]$ color-color plot for the spiral galaxies (black circles), ellipticals/S0 (open magenta diamonds), and irregular/Sm galaxies (blue). The colors of quasars (red circles) and interstellar dust (filled green diamonds) are also shown. Stellar photospheres are expected to lie at 0,0 on this plot. In $[8.0] - [24]$, the reddest and second reddest Irr/Sm galaxies are NGC 5408 and Markarian 33, respectively, while the reddest elliptical is NGC 1266 (which has a high far-infrared luminosity—see Table 2). The elliptical NGC 1377 is at (1.25, 3.5), with colors similar to those of quasars. The bluest spiral galaxy is the SAa galaxy NGC 5494, while the bluest elliptical is NGC 4125.

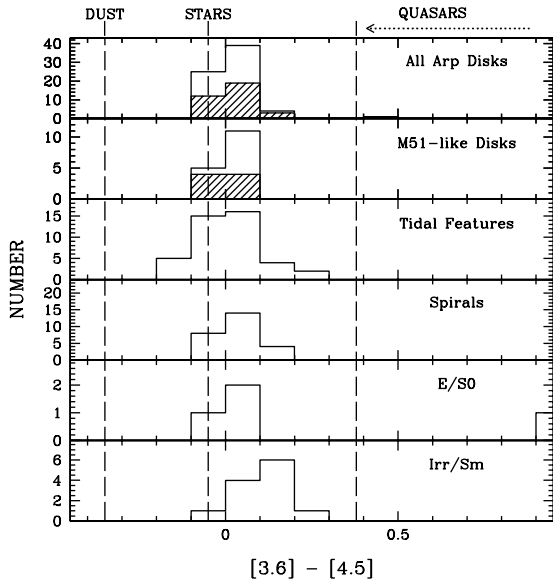


Fig. 21.— Histograms of the Spitzer IRAC $[3.6] - [4.5]$ colors for the different samples: the Arp galaxy main disks (top panel), the subset of M51-like systems (second panel), tidal features (third panel), the spiral galaxies (fourth panel), ellipticals/S0 (fifth panel), and irregular/Sm galaxies (bottom panel). The hatched galaxies are the more massive in the pair. The filled regions represent upper limits. The mean $[3.6] - [4.5]$ color for the Whitney et al. (2004) field stars is -0.05 , while the predicted value for interstellar dust is -0.35 (Li & Draine 2001). The Arp disk with the very red color of 0.44 is the Seyfert NGC 7469 (Arp 298S), while the red elliptical is NGC 1377. These colors are close to the colors of quasars (Hatziminaoglou et al. 2005).

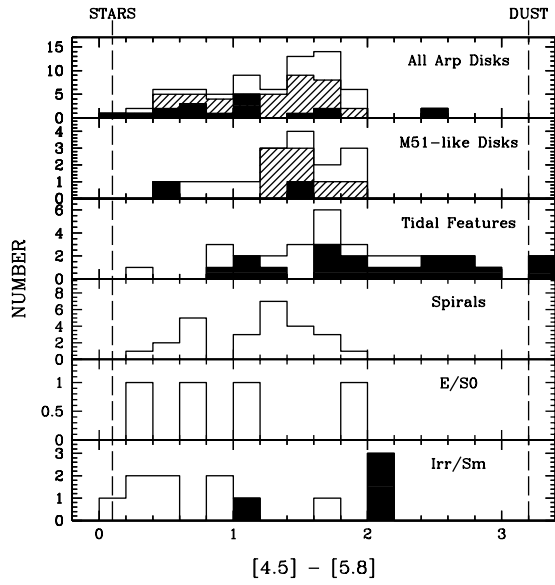


Fig. 22.— Histograms of the Spitzer IRAC $[4.5] - [5.8]$ colors for the different samples. The filled regions represent upper limits. The hatched galaxies are the more massive in the pair. The mean $[4.5] - [5.8]$ color for the Whitney et al. (2004) field stars is 0.1 , while the predicted value for interstellar dust is 3.2 (Li & Draine 2001).

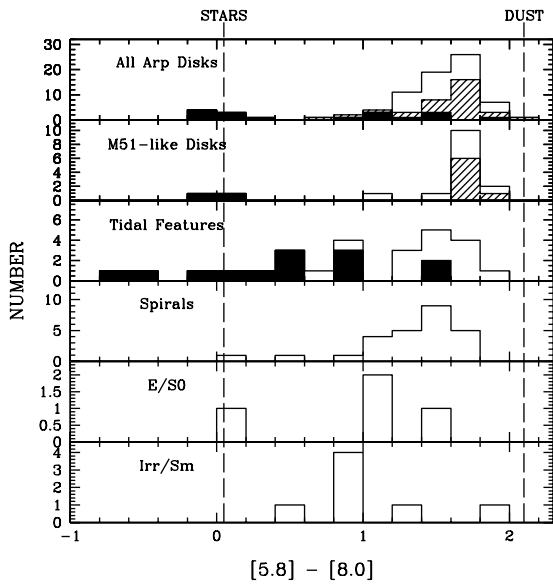


Fig. 23.— Histograms of the Spitzer IRAC $[5.8] - [8.0]$ colors for the different samples. The filled areas represent *lower* limits. The hatched galaxies are the more massive in the pair. The mean $[5.8] - [8.0]$ color for the Whitney et al. (2004) field stars is 0.05, while the predicted value for interstellar dust is 2.1 (Li & Draine 2001).

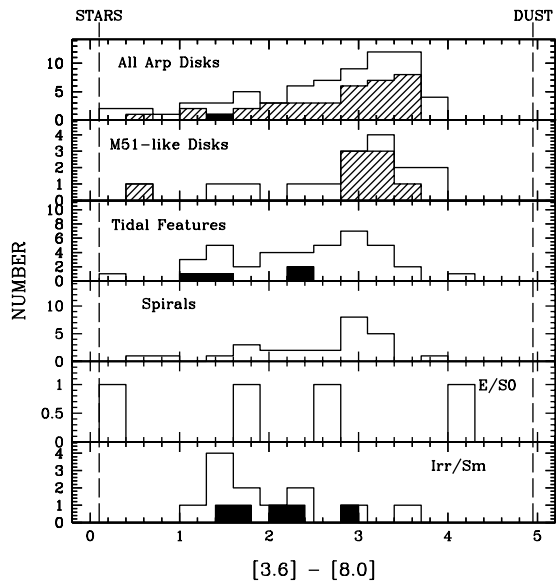


Fig. 24.— Histograms of the Spitzer IRAC $[3.6] - [8.0]$ colors for the different samples. The filled areas represent *upper* limits. The hatched galaxies are the more massive in the pair. The mean $[3.6] - [8.0]$ color for the Whitney et al. (2004) field stars is 0.1, while the predicted value for interstellar dust is 4.95 (Li & Draine 2001).

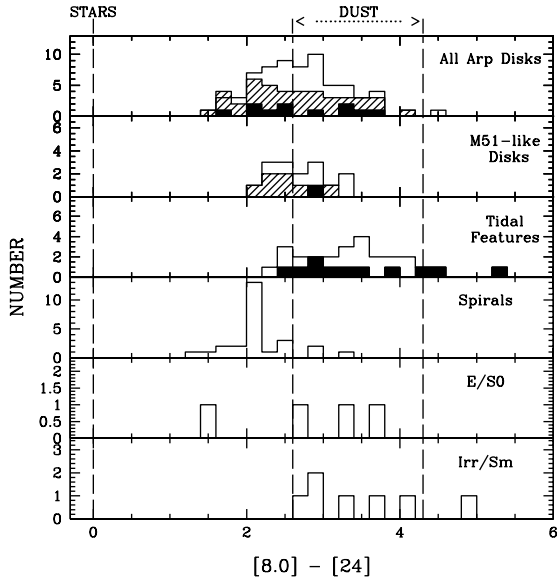


Fig. 25.— Histograms of the Spitzer IRAC $[8.0] - [24]$ colors for the different samples. The filled areas represent upper limits. The hatched galaxies are the more massive in the pair. The expected $[8.0] - [24]$ color for dust varies from 2.6 – 4.3 (Li & Draine 2001), increasing with increasing interstellar radiation field intensity, while stars are expected to be at ~ 0.0 .

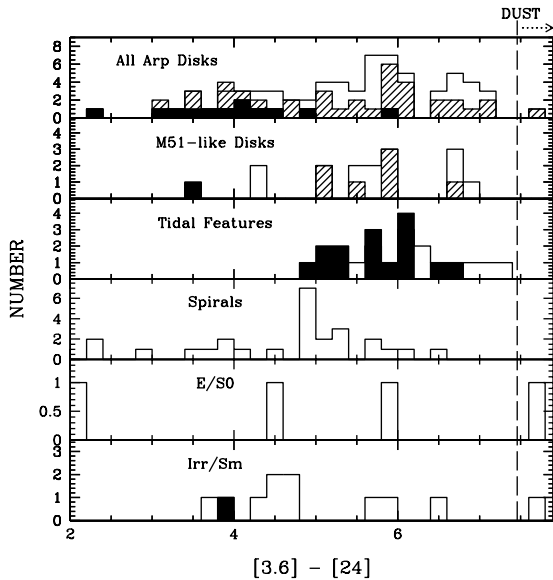


Fig. 26.— Histograms of the Spitzer IRAC $[3.6] - [24]$ colors for the different samples. The shaded galaxies are the more massive in the pair. The expected $[3.6] - [24]$ color for dust varies from 7.5 – 9.3 (Li & Draine 2001), increasing with increasing interstellar radiation field intensity, while stars are expected to be at ~ 0.0 .

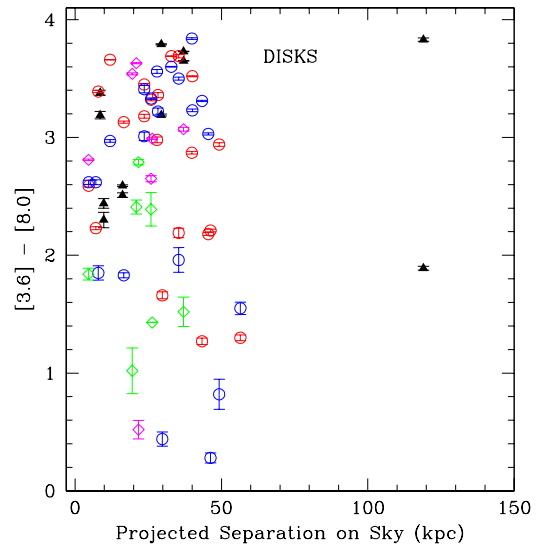


Fig. 27.— Projected pair separation vs. $[3.6] - [8.0]$ color, for the main disks in the galaxy pairs. Black triangles represent pairs with $3.6 \mu\text{m}$ luminosity ratios greater than 0.75 (i.e., close to equal mass pairs). Red and blue circles represent the more and less massive galaxy, respectively, in a pair with $3.6 \mu\text{m}$ luminosity ratios between 0.1 and 0.75 (i.e., intermediate mass ratio pairs). Magenta and green diamonds show the locations of the more and less massive galaxy, respectively, in pairs with $3.6 \mu\text{m}$ luminosity ratios less than 0.1 (i.e., highly unequal mass pairs).

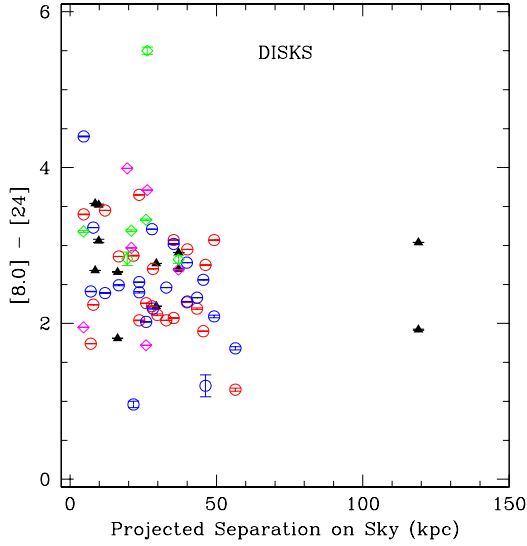


Fig. 28.— Projected pair separation vs. $[8.0] - [24]$ color, for the main disks in the galaxy pairs. The symbols are the same as in Figure 24.

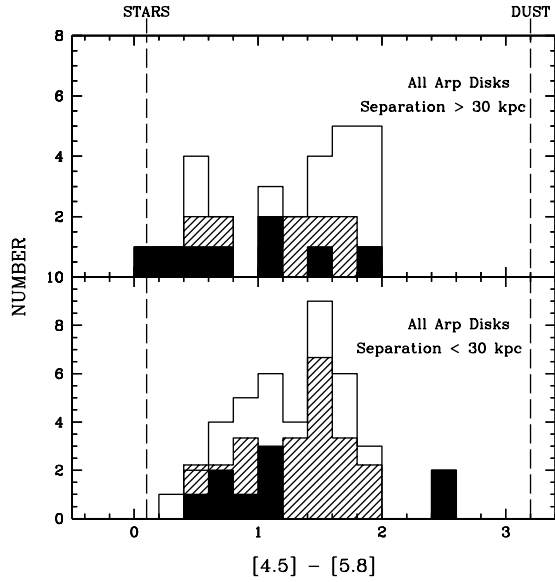


Fig. 30.— Histograms of the $[4.5] - [5.8]$ color for the close and wide pairs in our sample. The hatched regions mark galaxies are the more massive in the pair. The filled-in areas are upper limits.

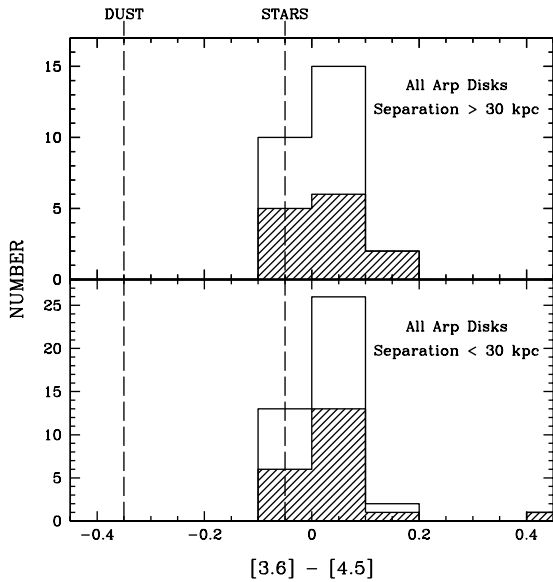


Fig. 29.— Histograms of the $[3.6] - [4.5]$ color for the close and wide pairs in our sample. The hatched galaxies are the more massive in the pair.

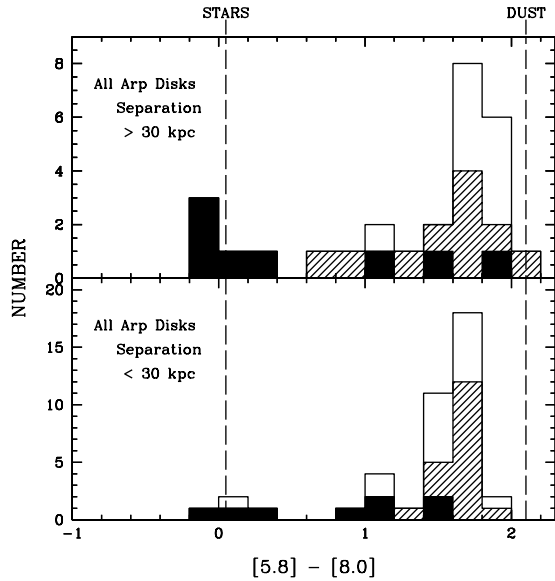


Fig. 31.— Histograms of the $[5.8] - [8.0]$ color for the close and wide pairs in our sample. The hatch-marked galaxies are the more massive in the pair. The filled-in areas indicate *lower* limits.

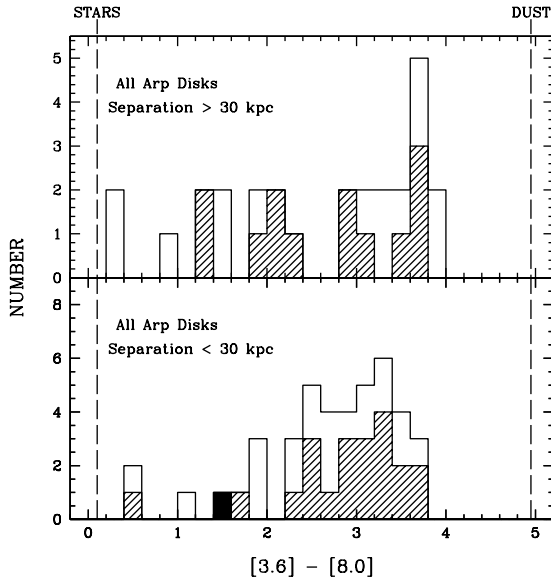


Fig. 32.— Histograms of the $[3.6] - [8.0]$ color for the close and wide pairs in our sample. The hatch-marked galaxies are the more massive in the pair. The filled-in regions indicate upper limits.

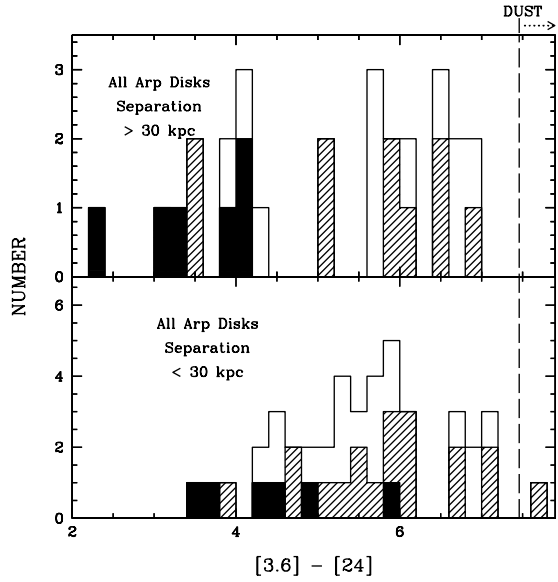


Fig. 34.— Histograms of the $[3.6] - [24]$ color for the close and wide pairs in our sample. The hatched regions indicate galaxies are the more massive in the pair. The filled-in regions indicate upper limits.

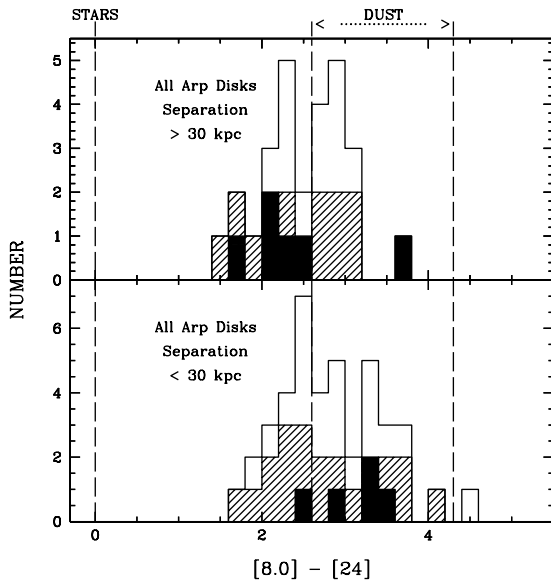


Fig. 33.— Histograms of the $[8.0] - [24]$ color for the close and wide pairs in our sample. The hatched regions indicate galaxies are the more massive in the pair. The filled-in regions indicate upper limits.

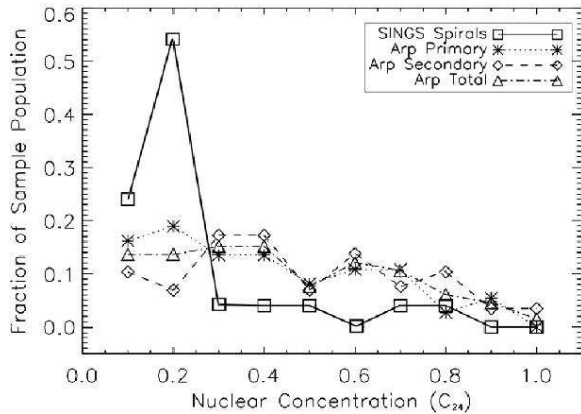


Fig. 35.— The fraction of sample population vs. central concentration, for the spirals and Arp disks. See text for more details.

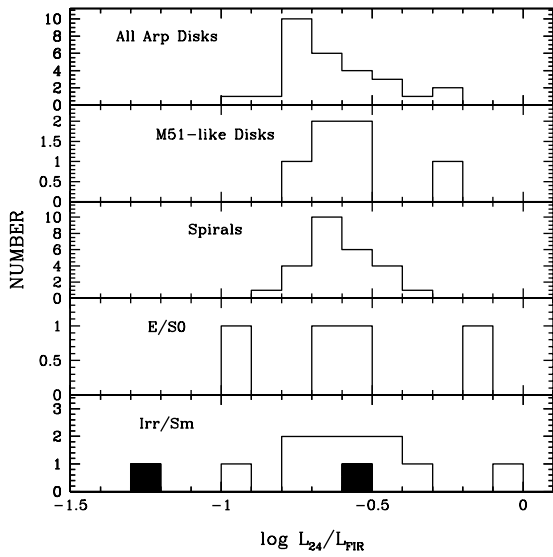


Fig. 36.— Histograms of the L_{24}/L_{FIR} ratios for the Arp galaxies (both disks combined), the M51-like systems (both galaxies), the spirals, Irr/Sm, and E/S0 galaxies. Upper limits are indicated by filled regions.

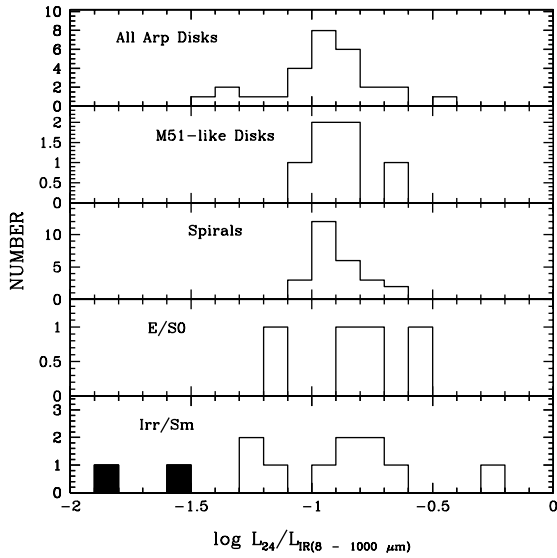


Fig. 37.— Histograms of the L_{24}/L_{IR} ratios for the Arp galaxies (both disks combined), the M51-like systems (both galaxies), the spirals, Irr/Sm, and E/S0 galaxies. The total $8 - 1000 \mu\text{m}$ luminosities L_{IR} are calculated as in Perault (1987), Kennicutt (1998), and Sanders & Mirabel (1996). Upper limits are indicated by filled regions.

TABLE 1
INTERACTING GALAXY SAMPLE

System	Other Names	Distance (Mpc)	Separation (kpc)	LOG L(FIR) ^a (L _⊙)	Notes on Morphology	Nuclear Spectral Types
Arp 24	NGC 3445	29.1	9.6	9.51	M51-like, but weak bridge	HII ^b
Arp 34	NGC 4613/4/5	67.2	43.4	10.07	equal mass spirals, short tails, small 3rd galaxy	–
Arp 65	NGC 90/93	69.5	56.5	9.53	widely separated pair	–
Arp 72	NGC 5994/6	46.9	21.0	10.19	M51-like	LINER+HII ^b
Arp 82	NGC 2535/6	57.0	28.3	10.18	M51-like	HII/HII ^c , LINER/HII ^b
Arp 84	NGC 5394/5	50.0	28	10.66	M51-like, but bridge from smaller galaxy	HII/LINER ^{b,c}
Arp 85	M51, NGC 5194/5	6.2	8.0	9.71	M51; spiral w/ small companion, bridge	LINER/HII ^{b,c}
Arp 86	NGC 7752/3	66.5	39.9	10.66	M51-like	HII/LINER ^c
Arp 87	NGC 3808	97.3	29.4	–	M51-like, but near-equal mass	LINER/HII ^{b,c}
Arp 89	NGC 2648	31.1	21.7	–	M51-like	–
Arp 104	NGC 5216/8	42.1	49.2	10.34	unequal mass spiral pair, long bridge	no emission/no emission ^b
Arp 107	UGC 5984	142.8	46.3	–	ring-like spiral w/ small E, bridge, short tail	Seyfert ^c
Arp 136	NGC 5820/1	47.6	50.7	8.89	equal mass, short tail ^d	–
Arp 181	NGC 3212/5	128.9	45.5	10.60	two close equal mass spirals, long tail	–
Arp 202	NGC 2719	44.0	4.7	9.75	unequal mass pair	HII/HII ^c
Arp 205	NGC 3448/UGC6016	23.0	26.4	9.77	peculiar, tails, small irregular companion	–
Arp 240	NGC 5257/8	91.0	37.1	11.19	close unequal mass spiral pair, short tail	HII/HII ^c , HII+LINER/HII ^b
Arp 242	NGC 4676	91.3	16.6	10.60	The Mice; equal mass spiral pair, long tails	LINER/LINER ^c , no emission ^b
Arp 244	NGC 4038/9	26.8	8.6	10.76	The Antennae; equal mass pair, long tails	HII/HII ^c , HII/HII+LINER ^b
Arp 253	UGC 173/4	29.0	9.8	8.68	two close spirals, short tails	HII ^b
Arp 271	NGC 5426/7	39.0	26	10.48	close equal mass spirals, bridge, no tails	HII/Seyfert ^{b,c}
Arp 279	NGC 1253	22.6	26.0	9.44	unequal mass close spiral pair	HII ^c
Arp 280	NGC 3769	11.5	4.6	8.85	unequal mass spirals, short tails	–
Arp 282	NGC 169	59.6	7.1	9.96	close pair	no emission/HII+LINER ^c
Arp 283	NGC 2798/9	26.3	12.0	10.35	two close spirals; tails+bridge	HII/HII ^c , HII/HII+LINER ^b
Arp 284	NGC 7714/5	35.3	19.5	10.30	unequal mass pair, partial ring, tails, bridge	HII/HII ^{b,c}
Arp 285	NGC 2854/6	39.1	40.1	9.93	equal mass widely separated spirals	–
Arp 290	IC 195/6	47.0	29.8	9.17	unequal mass separated spirals	HII/LINER ^c
Arp 293	NGC 6285/6	76.1	32.9	11.03	two equal mass separated spirals, tails	–
Arp 294	NGC 3786/8	40.2	16.2	–	equal mass close spiral pair, long tail	no emission ^{b,c}
Arp 295	Arp 295	87.8	119.0	10.83	wide unequal mass pair, long bridge	LINER/HII ^c
Arp 297N	NGC 5753/5	130.8	40.0	–	spiral with small companion	HII ^c
Arp 297S	NGC 5752/4	63.6	35.4	10.17	spiral with small companion	HII ^c
Arp 298	NGC 7469/IC5283	63.1	23.6	11.22	disk galaxies w/ ring, disturbed companion	Seyfert/HII ^c
NGC 4567	NGC 4567	35.5	12.3	–	two close spirals, no tails	–

^aIncludes the IRAS flux from both galaxies in the pair.

^bNuclear spectral type from Dahari (1985).

^cNuclear spectral type from Keel et al. (1985).

^dThe bright galaxy in the Arp (1966) Atlas photograph of Arp 136 is NGC 5820. This galaxy has a nearby similar-mass companion NGC 5821 at the same redshift, outside of the Arp Atlas field of view. The second small galaxy in the Arp Atlas image is a background galaxy.

TABLE 2
NORMAL GALAXY SAMPLE

Name	Type	Distance (Mpc)	LOG L(FIR) (L_{\odot})
Spiral Galaxies			
NGC 24	SAC	8.2	8.26
NGC 337	SBd	24.7	10.02
NGC 628	SAC	11.4	9.75
NGC 925	SABd	10.1	9.22
NGC 1097	SBb	16.9	10.43
NGC 1291	SBa	9.7	8.61
NGC 2403	SABcd	3.5	9.00
NGC 2841	SAb	9.8	9.00
NGC 3049	SBab	19.6	9.24
NGC 3184	SABcd	8.6	9.17
NGC 3521	SABbc	9.0	9.90
NGC 3621	Sad	6.2	9.36
NGC 3938	SAC	12.2	9.48
NGC 4254	SAC	20.0	10.47
NGC 4321	SABbc	20.0	10.33
NGC 4450	SAab	20.0	9.21
NGC 4559	SABcd	11.6	9.44
NGC 4579	SABb	20.0	9.76
NGC 4594	SAa	13.7	9.27
NGC 4725	SABab	17.1	9.56
NGC 4736	SAab	5.3	9.53
NGC 4826	SAab	5.6	9.34
NGC 5055	SAbc	8.2	9.81
NGC 6946	SABcd	5.5	9.87
NGC 7331	SAb	15.7	10.34
NGC 7793	SAd	3.2	8.61
Elliptical/S0 Galaxies			
NGC 855	E	9.6	8.42
NGC 1377	S0	24.4	9.77
NGC 3773	SA0	12.9	8.60
NGC 4125	E6p	21.4	8.80
Irregular/Sm Galaxies			
DDO 53	Im	3.5	6.77
DDO 154	IBm	5.4	<6.72
DDO 165	Im	3.5	<6.35
Holmberg II	Im	3.5	7.43
IC 4710	SBm	8.5	8.16
Markarian 33	Im	21.7	9.53
NGC 1705	Am	5.8	7.83
NGC 2915	I0	2.7	7.06
NGC 4236	SBdm	3.5	7.99
NGC 5398	SBdm	15.0	8.77
NGC 5408	IBm	4.5	7.91
NGC 6822	IBm	0.6	6.65

TABLE 3
STATISTICS ON IRAS FAR-INFRARED LUMINOSITIES

Type	Number	log L(FIR) ^a			log L(IR) ^b		
		median	mean	rms	median	mean	rms
Arp Galaxies ^c	29	10.18	10.10	0.69	10.48	10.43	0.64
M51-like Disks ^c	7	10.18	10.14	0.43	10.43	10.43	0.44
Spirals	26	9.44	9.50	0.57	9.72	9.78	0.57
E/S0	4	8.60	8.90	0.60	8.84	9.17	0.68
Irr/Sm	12	7.43	7.60	0.95	7.72	7.87	1.00

^aFar-infrared (40 – 120 μm) luminosities calculated as in Lonsdale et al. (1985) and Persson & Helou (1987).

^bTotal 8 – 1000 μm luminosity, calculated as in Perault (1987), Sanders et al. (1988), and Kennicutt (1998).

^cThe luminosities for the Arp galaxies include the combined fluxes from both galaxies in the pair.

TABLE 4
IRAC/MIPS24 OBSERVATIONAL PARAMETERS

Galaxy	RA (J2000)	Dec (J2000)	IRAC		MIPS24		On-source Time (sec)				
			Obs. Date	AORKEY	Obs. Date	AORKEY	3.6 μm	4.5 μm	5.8 μm	8.0 μm	24 μm
Arp 65	0:21:59.00	22:24:26.0	2004-12-14	10532352	2004-12-24	10540544	48	48	48	48	312
Arp 282	0:36:48.70	23:58:47.5	2004-12-16	10529536	2004-12-24	10539008	276	276	276	276	312
Arp 290	2:03:48.00	14:43:34.0	2005-01-15	10533376	2005-01-26	10542080	48	48	48	48	312
Arp 279	3:14:16.10	-2:48:42.0	2005-01-17	10529024	2005-01-31	10538496	48	...	48	...	312
			2005-01-17	10531072			...	48	...	48	...
Arp 82	8:11:13.70	25:12:10.0	2004-11-01	10526464	2005-04-02	10534656	72	...	72	...	312
			2004-11-01	10532096			...	72	...	72	...
Arp 89	8:42:39.81	14:17:08.0	2005-05-06	10527232	2004-11-05	10536704	24	...	24	24	312
			2005-05-06	10531840			...	24	...	24	...
Arp 202	9:00:15.64	35:43:25.5	2005-05-10	10528256	2004-11-02	10537728	276	276	276	276	312
Arp 253	9:43:25.00	-5:16:52.0	2004-12-17	10528768	2004-11-06	10541824	48	48	48	48	312
Arp 285	9:24:09.60	49:13:34.0	2005-05-06	10533120	2004-12-04	10538240	276	276	276	276	312
Arp 181	10:28:26.40	79:49:18.3	2004-12-16	10528000	2004-11-09	10537472	276	276	276	276	312
Arp 107	10:52:16.70	30:03:55.0	2004-12-17	10527488	2004-12-03	10536960	276	276	276	276	312
Arp 205	10:54:32.60	54:17:54.0	2004-12-16	10531328	2004-11-10	10540800	48	48	48	48	312
Arp 24	10:54:40.50	56:59:04.4	2004-12-16	10525952	2004-11-10	10535168	276	276	276	276	312
Arp 280	11:37:47.30	47:53:10.0	2004-12-17	10529280	2004-12-03	10538752	276	276	276	276	312
Arp 294	11:39:43.59	31:55:12.4	2004-12-17	10529792	2005-05-12	10539264	276	276	276	276	312
Arp 87	11:40:44.40	22:26:16.0	2004-12-18	10526976	2005-05-18	10536448	276	276	276	276	312
NGC 4567	12:36:32.70	11:15:28.3	2005-06-10	10530816	2005-01-28	10540032	84	...	84	...	312
			2005-06-10	10530560			...	84	...	84	...
Arp 34	12:41:34.00	26: 3:31.0	2005-06-09	10532608	2005-01-27	10535424	108	108	108	108	312
Arp 104	13:32:08.90	62:44:02.0	2004-11-25	10531584	2004-12-02	10540288	48	48	48	48	312
Arp 240	13:39:55.20	0:50:13.0			2005-02-02	10537984	312
Arp 84	13:58:35.80	37:26:20.0			2005-01-25	10541312	312
Arp 271	14:03:25.50	-6:02:60.0	2005-07-21	10532864	2005-08-02	10541568	36	36	36	36	312
Arp 297	14:45:19.40	38:45:10.8	2005-01-21	10530304	2005-01-29	10539776	276	276	276	276	312
Arp 136	14:58:39.82	53:53:09.9	2004-12-21	10527744	2004-12-26	10537216	48	48	48	48	312
Arp 72	15:46:56.03	17:52:43.2	2005-03-27	10526208	2005-03-10	10534912	276	276	276	276	312
Arp 295	23:41:54.10	-3:38:29.0	2004-11-26	10530048	2004-11-29	10539520	48	48	48	48	312
Arp 86	23:47:01.90	29:28:23.7			2004-12-06	10536192	312

TABLE 5
SPITZER FLUX DENSITIES FOR INTERACTING GALAXY SAMPLE

Arp Name	Component	Other Name	F _{3.6μm} (mJy)	F _{4.5μm} (mJy)	F _{5.8μm} (mJy)	F _{8.0μm} (mJy)	F _{24μm} (mJy)
Arp 24	E	UGC 6021	1.16 ± 0.02	0.77 ± 0.04	≤ 2.0	1.1 ± 0.1	1.6 ± 0.4
Arp 24	MAIN	NGC 3445	28.3 ± 0.2	18.6 ± 0.4	44.5 ± 7.3	109.4 ± 1.4	151.9 ± 4.7
Arp 34	NE	NGC 4615	12.49 ± 0.04	8.14 ± 0.04	21.7 ± 0.6	59.5 ± 0.2	58.8 ± 2.0
Arp 34	NE E TAIL	NGC 4615 EAST TAIL	3.54 ± 0.01	2.44 ± 0.01	7.5 ± 0.2	21.23 ± 0.06	38.5 ± 0.7
Arp 34	NE W TAIL	NGC 4615 WEST TAIL	2.36 ± 0.01	1.54 ± 0.01	4.3 ± 0.2	11.88 ± 0.05	11.8 ± 0.5
Arp 34	NW SMALL	NGC 4613	6.49 ± 0.03	4.04 ± 0.03	6.7 ± 0.4	15.4 ± 0.1	19.8 ± 1.3
Arp 34	S	NGC 4614	27.8 ± 0.1	18.0 ± 0.1	19.1 ± 1.7	20.5 ± 0.5	17.3 ± 5.5
Arp 65	E	NGC 93	61.5 ± 0.2	36.5 ± 0.1	34.7 ± 1.9	46.4 ± 1.1	≤ 25.9
Arp 65	N TAIL	NGC 90 TAIL	0.74 ± 0.07	0.45 ± 0.05	≤ 1.9	1.7 ± 0.4	≤ 9.6
Arp 65	S TAIL	NGC 90 TAIL	0.73 ± 0.05	0.47 ± 0.03	≤ 1.4	1.8 ± 0.3	≤ 6.9
Arp 65	W	NGC 90	20.5 ± 0.2	12.4 ± 0.1	12.0 ± 1.7	19.5 ± 0.9	≤ 23.2
Arp 72	BRIDGE	NGC 5994/6 BRIDGE	6.9 ± 0.2	4.5 ± 0.2	11.6 ± 1.6	30.7 ± 0.6	42.6 ± 1.6
Arp 72	E	NGC 5996	30.8 ± 0.1	20.8 ± 0.1	71.2 ± 1.2	199.0 ± 0.4	364.5 ± 1.0
Arp 72	E TAIL	NGC 5996 TAIL	4.6 ± 0.1	3.1 ± 0.1	8.1 ± 1.2	13.9 ± 0.4	38.2 ± 1.2
Arp 72	W	NGC 5994	2.45 ± 0.08	1.65 ± 0.06	2.2 ± 0.7	5.1 ± 0.2	11.5 ± 0.7
Arp 82	BRIDGE	NGC 2535/6 BRIDGE	0.83 ± 0.07	0.51 ± 0.06	≤ 4.7	3.7 ± 0.4	≤ 5.3
Arp 82	N	NGC 2535	43.7 ± 0.6	28.5 ± 0.5	78.1 ± 13.1	220.2 ± 3.2	261.6 ± 13.4
Arp 82	S	NGC 2536	10.6 ± 0.2	6.9 ± 0.2	17.1 ± 4.0	46.9 ± 1.0	43.0 ± 4.2
Arp 84	N	NGC 5394	46.2 ± 0.3	30.9 ± 0.3	102.0 ± 2.7	279.8 ± 3.8	633.4 ± 12.8
Arp 84	N TAIL	NGC 5394 TAIL	1.86 ± 0.09	1.2 ± 0.1	≤ 2.7	≤ 3.9	≤ 13.4
Arp 84	S	NGC 5395	154.4 ± 0.9	97.0 ± 1.1	221.2 ± 8.9	548.1 ± 12.4	434.2 ± 40.2
Arp 85	N	NGC 5195	1077.8 ± 3.1	676.9 ± 5.6	848.6 ± 136.5	1351.6 ± 75.6	1505.6 ± 89.2
Arp 85	S	NGC 5194	2707.4 ± 4.4	1732.0 ± 7.9	5403.8 ± 191.8	14023.6 ± 106.2	16970.6 ± 125.1
Arp 86	BRIDGE	NGC 7752/3 BRIDGE	5.45 ± 0.08	3.59 ± 0.04	8.2 ± 0.8	19.9 ± 0.5	20.2 ± 3.3
Arp 86	N	NGC 7753	112.9 ± 0.5	70.2 ± 0.3	140.8 ± 5.3	362.1 ± 3.5	338.6 ± 19.5
Arp 86	S	NGC 7752	22.5 ± 0.1	15.37 ± 0.06	61.5 ± 1.2	176.5 ± 0.7	269.0 ± 4.2
Arp 87	BRIDGE	NGC 3808 BRIDGE	1.47 ± 0.02	0.93 ± 0.03	2.4 ± 0.4	5.5 ± 0.2	0.0
Arp 87	N	NGC 3808B	14.88 ± 0.04	10.44 ± 0.08	36.0 ± 1.1	111.4 ± 0.4	169.7 ± 2.0
Arp 87	S	NGC 3808A	15.02 ± 0.05	9.70 ± 0.09	21.9 ± 1.3	64.7 ± 0.5	58.8 ± 2.5
Arp 87	SMALL N		0.32 ± 0.01	0.20 ± 0.02	≤ 0.7	1.20 ± 0.09	2.0 ± 0.6
Arp 87	S TAIL	NGC 3808A TAIL	0.37 ± 0.01	0.25 ± 0.02	≤ 1.0	0.9 ± 0.1	≤ 0.0
Arp 89	E	KPG 168	7.74 ± 0.09	5.0 ± 0.1	9.1 ± 2.9	23.1 ± 0.4	40.7 ± 3.7
Arp 89	E TAIL		0.77 ± 0.05	0.44 ± 0.09	≤ 5.3	≤ 0.64 0	≤ 5.4
Arp 89	W	NGC 2648	130.8 ± 0.9	78.4 ± 1.4	≤ 81.8	48.6 ± 3.5	≤ 83.5
Arp 104	BRIDGE	NGC 5216/8 BRIDGE	4.2 ± 0.4	3.2 ± 0.4	≤ 18.2	4.0 ± 1.1	–
Arp 104	N	NGC 5218	86.4 ± 0.9	56.8 ± 0.9	122.7 ± 15.3	295.7 ± 2.7	604.9 ± 8.1
Arp 104	N TAIL	NGC 5218 TAIL	2.1 ± 0.3	1.6 ± 0.3	≤ 13.0	≤ 2.3	–
Arp 104	S	NGC 5216	47.0 ± 0.9	28.7 ± 0.9	≤ 46.2	22.8 ± 2.7	≤ 23.2
Arp 107	BRIDGE	UGC 5984 BRIDGE	1.39 ± 0.02	0.84 ± 0.04	≤ 1.6	1.36 ± 0.05	≤ 4.1
Arp 107	N	UGC 5984N	10.29 ± 0.06	6.2 ± 0.1	≤ 4.5	3.0 ± 0.1	≤ 10.4
Arp 107	N TAIL	UGC 5984N TAIL	1.23 ± 0.04	0.84 ± 0.07	≤ 2.6	0.38 ± 0.07	≤ 6.2
Arp 107	S	UGC 5984S	17.9 ± 0.1	11.3 ± 0.2	≤ 9.7	31.5 ± 0.2	50.8 ± 7.3
Arp 107	W TAIL	UGC 5984S TAIL	0.71 ± 0.02	0.42 ± 0.04	≤ 1.5	0.51 ± 0.05	≤ 3.8
Arp 136	NW	NGC 5821	15.6 ± 0.2	–	30.2 ± 7.3	–	15.6 ± 2.0
Arp 136	SW	NGC 5820	83.3 ± 0.5	49.0 ± 0.6	≤ 53.1	25.5 ± 1.0	≤ 18.1
Arp 181	E	NGC 3215	29.1 ± 0.2	17.8 ± 0.3	≤ 20.9	49.5 ± 0.5	32.3 ± 2.2
Arp 181	W	NGC 3212	20.7 ± 0.1	13.4 ± 0.2	23.8 ± 5.3	77.1 ± 0.4	96.8 ± 1.8
Arp 181	W TAIL	NGC 3212 TAIL	1.2 ± 0.1	0.6 ± 0.1	≤ 10.8	1.4 ± 0.3	–
Arp 202	N	NGC 2719	9.05 ± 0.05	6.06 ± 0.07	8.6 ± 2.0	22.4 ± 0.2	62.8 ± 4.3
Arp 202	S	NGC 2719A	3.88 ± 0.04	2.69 ± 0.06	≤ 4.8	9.9 ± 0.1	67.6 ± 3.1
Arp 205	BRIDGE	NGC 3448/UGC6016 BRIDGE	1.8 ± 0.2	1.3 ± 0.2	≤ 10.0	3.0 ± 0.6	≤ 4.7
Arp 205	E	NGC 3448	74.6 ± 0.3	50.0 ± 0.4	119.3 ± 7.1	264.8 ± 1.2	941.2 ± 3.1
Arp 205	E TAIL	NGC 3448 TAIL	0.8 ± 0.1	0.6 ± 0.2	≤ 8.5	≤ 1.5	≤ 3.8
Arp 205	W	UGC 6016	2.0 ± 0.2	1.4 ± 0.2	≤ 9.8	≤ 1.7	≤ 4.3
Arp 240	BRIDGE	NGC 5257/8 BRIDGE	3.26 ± 0.07	2.1 ± 0.1	≤ 14.7	18.0 ± 0.6	65.7 ± 6.4
Arp 240	E	NGC 5258	52.55 ± 0.06	35.53 ± 0.09	111.9 ± 4.6	345.8 ± 0.5	503.2 ± 5.9
Arp 240	E TAIL	NGC 5258 TAIL	2.71 ± 0.05	1.72 ± 0.08	≤ 10.4	12.2 ± 0.4	≤ 13.9

TABLE 5—Continued

Arp Name	Component	Other Name	F _{3.6μm} (mJy)	F _{4.5μm} (mJy)	F _{5.8μm} (mJy)	F _{8.0μm} (mJy)	F _{24μm} (mJy)
Arp 240	W	NGC 5257	46.62 ± 0.08	31.5 ± 0.1	106.8 ± 5.6	330.3 ± 0.6	572.4 ± 7.5
Arp 240	W TAIL	NGC 5257 TAIL	0.90 ± 0.02	0.57 ± 0.03	≤ 4.6	3.0 ± 0.2	≤ 6.6
Arp 242	N	NGC 4676A	28.6 ± 0.2	19.3 ± 0.1	45.4 ± 7.9	116.6 ± 0.5	187.8 ± 6.2
Arp 242	N TAIL	NGC 4676A TAIL	6.1 ± 0.2	3.8 ± 0.1	≤ 18.7	9.6 ± 0.4	—
Arp 242	S	NGC 4676 BRIDGE	20.3 ± 0.2	12.5 ± 0.1	≤ 20.7	25.1 ± 0.4	32.0 ± 5.3
Arp 242	S TAIL	NGC 4676 BRIDGE TAIL	2.3 ± 0.1	1.31 ± 0.09	≤ 14.7	1.9 ± 0.3	≤ 0.0
Arp 244	N	NGC 4038	299.6 ± 1.2	191.7 ± 1.6	609.1 ± 45.3	1523.6 ± 29.4	1948.5 ± 26.6
Arp 244	N TAIL	NGC 4038 TAIL	8.7 ± 0.5	5.9 ± 0.7	≤ 55.0	≤ 36.2	—
Arp 244	S	NGC 4039	291.4 ± 1.5	198.9 ± 2.0	520.8 ± 54.9	1255.6 ± 36.4	4108.6 ± 31.8
Arp 244	S TAIL	NGC 4039 TAIL	7.5 ± 1.3	≤ 5.14 0	≤ 143.4	≤ 92.7	≤ 0.0
Arp 253	E	UGCA 174	2.38 ± 0.05	1.57 ± 0.07	≤ 3.0	4.5 ± 0.3	7.9 ± 2.1
Arp 253	W	UGCA 173	3.11 ± 0.05	2.10 ± 0.06	≤ 2.8	6.7 ± 0.2	16.8 ± 1.8
Arp 271	N	NGC 5427	155.8 ± 0.9	103.4 ± 0.7	283.6 ± 6.8	749.6 ± 3.6	734.0 ± 17.4
Arp 271	S	NGC 5426	84.1 ± 0.4	54.3 ± 0.3	160.2 ± 2.8	412.0 ± 1.5	297.6 ± 7.2
Arp 279	NE	NGC 1253A	10.6 ± 0.4	7.1 ± 0.2	≤ 41.8	21.8 ± 2.7	≤ 62.2
Arp 279	SW	NGC 1253	108.8 ± 1.0	71.5 ± 0.5	110.8 ± 32.4	285.0 ± 6.4	213.6 ± 50.4
Arp 280	E	NGC 3769A	4.58 ± 0.06	3.09 ± 0.07	≤ 3.9	5.6 ± 0.3	10.9 ± 1.7
Arp 280	W	NGC 3769	90.5 ± 0.3	57.9 ± 0.3	117.1 ± 6.1	277.2 ± 1.2	186.1 ± 7.5
Arp 282	E TAIL	NGC 169 TAIL	4.1 ± 0.3	2.7 ± 0.2	≤ 3.6	7.9 ± 0.7	≤ 14.0
Arp 282	N	NGC 169	73.2 ± 0.5	45.1 ± 0.4	58.7 ± 2.2	129.1 ± 1.3	74.1 ± 7.7
Arp 282	S	NGC 169A	12.5 ± 0.2	7.8 ± 0.1	13.3 ± 0.7	31.5 ± 0.4	32.9 ± 2.6
Arp 283	BRIDGE	NGC 2798/9 BRIDGE	1.15 ± 0.03	0.72 ± 0.03	2.4 ± 0.7	5.5 ± 0.2	0.0
Arp 283	E	NGC 2799	14.34 ± 0.08	9.09 ± 0.09	23.8 ± 1.8	50.4 ± 0.4	52.2 ± 4.3
Arp 283	N TAIL	NGC 2798 NORTH TAIL	5.35 ± 0.05	3.18 ± 0.06	4.6 ± 1.3	4.6 ± 0.3	0.0
Arp 283	S TAIL	NGC 2798 SOUTH TAIL	2.21 ± 0.06	1.27 ± 0.06	≤ 4.1	3.8 ± 0.3	0.0
Arp 283	W	NGC 2798	111.83 ± 0.08	77.01 ± 0.09	288.9 ± 1.8	742.8 ± 0.4	2136.5 ± 4.5
Arp 284	BRIDGE	NGC 7714/5 BRIDGE	3.7 ± 0.3	2.2 ± 0.6	≤ 11.1	5.7 ± 1.3	—
Arp 284	E	NGC 7715	3.77 ± 0.10	2.3 ± 0.2	≤ 3.2	2.2 ± 0.4	≤ 5.6
Arp 284	E TAIL	NGC 7715 TAIL	1.5 ± 0.1	0.8 ± 0.2	≤ 2.9	≤ 1.1	—
Arp 284	W	NGC 7714	63.8 ± 0.4	42.7 ± 0.7	134.5 ± 4.9	382.7 ± 1.7	1826.8 ± 8.1
Arp 284	W TAIL	NGC 7714 TAIL	7.8 ± 0.3	4.6 ± 0.5	14.0 ± 3.0	26.0 ± 1.1	—
Arp 285	N	NGC 2856	61.5 ± 0.2	41.55 ± 0.08	128.4 ± 3.6	362.1 ± 0.8	616.2 ± 2.1
Arp 285	N TAIL	NGC 2856 TAIL	0.47 ± 0.03	0.39 ± 0.02	2.0 ± 0.6	5.4 ± 0.2	6.3 ± 0.4
Arp 285	S	NGC 2854	41.4 ± 0.3	26.2 ± 0.1	73.9 ± 6.1	184.9 ± 1.4	184.4 ± 3.6
Arp 290	N	IC 196	49.3 ± 0.3	30.4 ± 0.4	33.2 ± 5.0	51.9 ± 1.4	≤ 62.2
Arp 290	N TAIL	IC 196 TAIL	4.70 ± 0.06	2.98 ± 0.06	2.7 ± 0.8	5.2 ± 0.2	≤ 10.1
Arp 290	S	IC 195	29.4 ± 0.1	17.6 ± 0.2	15.3 ± 2.0	10.1 ± 0.6	≤ 24.5
Arp 293	BRIDGE	NGC 6285/6 BRIDGE	2.09 ± 0.05	1.35 ± 0.08	≤ 2.3	5.2 ± 0.3	15.9 ± 2.3
Arp 293	N	NGC 6285	17.40 ± 0.03	11.66 ± 0.06	36.0 ± 0.5	108.4 ± 0.2	115.3 ± 1.4
Arp 293	N TAIL	NGC 6285 TAIL	1.46 ± 0.02	0.91 ± 0.03	1.4 ± 0.3	4.4 ± 0.1	10.5 ± 0.9
Arp 293	S	NGC 6286	71.21 ± 0.06	52.3 ± 0.1	175.7 ± 1.0	486.2 ± 0.4	399.7 ± 2.8
Arp 293	S TAIL	NGC 6286 TAIL	2.19 ± 0.03	1.44 ± 0.06	5.8 ± 0.6	7.8 ± 0.2	16.8 ± 1.6
Arp 294	N	NGC 3788	76.0 ± 0.3	46.8 ± 0.3	83.3 ± 5.2	188.3 ± 1.1	115.3 ± 9.2
Arp 294	S	NGC 3786	76.7 ± 0.6	56.3 ± 0.7	88.9 ± 12.5	176.5 ± 2.8	240.8 ± 22.8
Arp 295	BRIDGE	ARP 295 BRIDGE	2.4 ± 0.6	≤ 2.22 0	≤ 18.4	2.8 ± 0.7	≤ 0.0
Arp 295	N	ARP 295B	31.4 ± 0.4	21.4 ± 0.5	81.8 ± 4.2	243.7 ± 0.5	498.5 ± 7.1
Arp 295	S	ARP 295A	39.9 ± 0.5	25.3 ± 0.5	29.7 ± 4.5	51.9 ± 0.5	23.9 ± 7.4
Arp 295	S TAIL	ARP 295A TAIL	2.8 ± 0.4	2.1 ± 0.5	≤ 13.0	2.1 ± 0.5	—
Arp 297	NE	NGC 5755	13.7 ± 0.1	10.1 ± 0.1	25.2 ± 5.3	93.5 ± 1.0	191.3 ± 2.5
Arp 297	NE N TAIL	NGC 5755 TAIL	0.98 ± 0.08	0.65 ± 0.08	≤ 11.8	2.7 ± 0.7	0.0
Arp 297	NW	NGC 5753	4.25 ± 0.07	2.77 ± 0.06	≤ 9.3	5.9 ± 0.6	≤ 4.7
Arp 297	SE	NGC 5754	37.4 ± 0.3	22.6 ± 0.3	≤ 40.2	64.1 ± 2.3	32.6 ± 6.1
Arp 297	SE TAIL S	NGC 5754 TAIL	1.14 ± 0.05	0.73 ± 0.05	≤ 6.7	2.8 ± 0.4	≤ 0.0
Arp 297	SW	NGC 5752	9.47 ± 0.06	6.46 ± 0.06	20.0 ± 2.8	54.3 ± 0.5	95.0 ± 1.3
Arp 298	N	IC 5283	31.4 ± 0.3	20.8 ± 0.8	60.4 ± 9.4	165.5 ± 4.5	196.7 ± 14.4
Arp 298	S	NGC 7469	187.3 ± 0.5	181.4 ± 1.3	449.5 ± 15.0	1025.3 ± 7.1	3263.6 ± 22.5
Arp 298	W TAIL	IC 5283 TAIL	3.0 ± 0.2	2.0 ± 0.5	≤ 17.4	≤ 8.4	—

TABLE 5—*Continued*

Arp Name	Component	Other Name	$F_{3.6\mu m}$ (mJy)	$F_{4.5\mu m}$ (mJy)	$F_{5.8\mu m}$ (mJy)	$F_{8.0\mu m}$ (mJy)	$F_{24\mu m}$ (mJy)
NGC 4567	N	NGC 4567N	143.4 ± 3.0	90.9 ± 2.1	203.6 ± 49.3	523.4 ± 13.0	734.0 ± 115.6
NGC 4567	S	NGC 4567S	429.1 ± 4.4	277.0 ± 3.1	732.3 ± 71.5	1831.7 ± 18.7	1666.1 ± 150.7

TABLE 6
SPITZER FLUX DENSITIES FOR NORMAL GALAXY SAMPLE

Galaxy	F _{3.6μm} (mJy)	F _{4.5μm} (mJy)	F _{5.8μm} (mJy)	F _{8.0μm} (mJy)	F _{24μm} (mJy)
Spiral Galaxies					
NGC 24	112.9 \pm 0.6	74.2 \pm 0.8	88.9 \pm 5.4	168.6 \pm 3.8	125.2 \pm 4.6
NGC 337	104.8 \pm 0.5	70.9 \pm 0.5	201.7 \pm 5.1	499.9 \pm 14.3	747.6 \pm 12.8
NGC 628	1010.5 \pm 9.8	749.1 \pm 13.8	1544.2 \pm 109.9	3791.9 \pm 557.0	3204.0 \pm 40.1
NGC 925	360.2 \pm 6.3	255.0 \pm 4.0	462.1 \pm 23.2	709.3 \pm 79.8	827.4 \pm 26.4
NGC 1097	1356.9 \pm 8.7	917.4 \pm 8.3	1891.0 \pm 25.9	4196.2 \pm 69.0	6511.8 \pm 19.8
NGC 1291	2293.8 \pm 11.7	1427.4 \pm 8.9	1369.9 \pm 36.3	868.7 \pm 75.3	498.5 \pm 40.6
NGC 2403	1943.4 \pm 36.0	1414.3 \pm 14.5	2835.9 \pm 60.2	5138.8 \pm 622.9	5830.4 \pm 53.2
NGC 2841	1382.1 \pm 5.0	829.0 \pm 4.6	992.4 \pm 38.0	1580.7 \pm 10.6	967.6 \pm 7.0
NGC 3049	44.9 \pm 0.4	29.5 \pm 0.3	71.2 \pm 4.7	170.2 \pm 3.0	434.2 \pm 1.6
NGC 3184	570.9 \pm 19.7	372.0 \pm 8.2	833.1 \pm 45.9	1733.2 \pm 88.9	1437.8 \pm 44.1
NGC 3521	2150.6 \pm 12.4	1388.5 \pm 12.1	2942.4 \pm 221.3	7635.9 \pm 303.4	5268.6 \pm 185.9
NGC 3621	1128.6 \pm 21.6	749.1 \pm 30.9	2131.6 \pm 85.1	4601.1 \pm 47.9	3449.0 \pm 24.8
NGC 3938	344.0 \pm 7.3	234.7 \pm 12.0	555.5 \pm 12.7	1376.8 \pm 15.8	1080.7 \pm 22.9
NGC 4254	738.8 \pm 11.8	499.5 \pm 8.0	1873.7 \pm 111.9	5331.6 \pm 55.8	4185.0 \pm 35.5
NGC 4321	1068.0 \pm 18.9	702.3 \pm 11.5	1805.9 \pm 95.9	4353.7 \pm 290.9	3386.1 \pm 30.9
NGC 4450	570.9 \pm 3.9	368.6 \pm 3.1	360.3 \pm 22.8	495.3 \pm 65.9	217.6 \pm 9.8
NGC 4559	449.3 \pm 18.6	321.0 \pm 15.3	598.0 \pm 50.1	1255.6 \pm 138.7	1121.2 \pm 41.1
NGC 4579	938.8 \pm 4.5	578.8 \pm 5.3	745.9 \pm 29.7	1093.6 \pm 43.0	812.3 \pm 43.8
NGC 4594	4135.7 \pm 16.8	2503.5 \pm 15.0	2315.8 \pm 75.0	2083.8 \pm 52.6	797.4 \pm 25.1
NGC 4725	1160.3 \pm 26.0	722.0 \pm 13.0	905.1 \pm 42.7	1640.1 \pm 131.4	827.4 \pm 28.9
NGC 4736	3737.2 \pm 75.2	2390.8 \pm 83.7	3878.8 \pm 307.5	6900.1 \pm 263.5	5466.4 \pm 66.5
NGC 4826	2633.6 \pm 19.3	1623.9 \pm 10.8	2073.5 \pm 83.0	3154.0 \pm 155.0	2521.7 \pm 41.6
NGC 5055	2658.0 \pm 14.9	1732.0 \pm 12.2	3808.0 \pm 74.0	8069.7 \pm 189.6	5830.4 \pm 34.4
NGC 6946	3986.1 \pm 61.6	2719.9 \pm 79.9	8029.7 \pm 416.7	18486.6 \pm 981.9	20030.8 \pm 435.5
NGC 7331	1822.0 \pm 13.5	1198.3 \pm 9.8	2610.3 \pm 61.7	5481.0 \pm 68.8	3960.0 \pm 40.9
NGC 7793	825.2 \pm 13.5	527.9 \pm 16.4	1369.9 \pm 83.2	2721.8 \pm 121.8	2078.3 \pm 19.5
Elliptical/S0 Galaxies					
NGC 855	48.8 \pm 0.7	32.4 \pm 0.6	41.4 \pm 3.6	63.5 \pm 7.8	84.3 \pm 5.0
NGC 1377	60.9 \pm 0.3	91.7 \pm 0.9	350.5 \pm 3.9	568.7 \pm 12.9	1760.8 \pm 6.0
NGC 3773	24.9 \pm 0.3	15.9 \pm 0.4	28.9 \pm 3.7	64.1 \pm 3.4	138.6 \pm 3.7
NGC 4125	732.1 \pm 2.7	468.3 \pm 4.9	360.3 \pm 7.6	234.9 \pm 5.0	106.1 \pm 8.4
Irregular/Sm Galaxies					
DDO 53	5.7 \pm 0.4	4.4 \pm 0.3	\leq 19.4	\leq 20.1	29.2 \pm 2.8
DDO 154	4.3 \pm 0.4	3.0 \pm 0.2	\leq 12.5	\leq 7.0	\leq 3.7
DDO 165	15.7 \pm 0.9	11.3 \pm 1.0	\leq 53.5	\leq 14.3	11.6 \pm 2.3
Holmberg II	94.7 \pm 4.6	70.2 \pm 3.9	66.8 \pm 10.6	\leq 167.1	169.7 \pm 24.5
IC 4710	76.0 \pm 3.5	52.3 \pm 4.1	57.1 \pm 10.7	77.1 \pm 12.4	114.2 \pm 10.1
Markarian 33	28.6 \pm 0.3	20.6 \pm 0.4	58.2 \pm 6.2	170.2 \pm 1.2	827.4 \pm 2.3
NGC 1705	28.1 \pm 0.2	19.9 \pm 0.4	17.9 \pm 5.8	24.4 \pm 1.4	52.7 \pm 2.2
NGC 2915	65.5 \pm 1.0	43.9 \pm 0.9	33.2 \pm 6.5	42.4 \pm 8.7	65.1 \pm 15.8
NGC 4236	280.9 \pm 23.4	171.6 \pm 28.2	\leq 328.6	\leq 293.0	485.0 \pm 28.9
NGC 5398	45.3 \pm 0.7	30.7 \pm 0.6	42.5 \pm 6.6	80.7 \pm 3.0	259.2 \pm 6.5
NGC 5408	39.9 \pm 1.5	28.7 \pm 1.3	26.3 \pm 8.0	36.5 \pm 3.1	388.8 \pm 5.0
NGC 6822	2293.8 \pm 361.8	1565.1 \pm 160.2	2424.9 \pm 571.1	2142.2 \pm 280.7	2949.2 \pm 222.5

TABLE 7
STATISTICS ON SPITZER LUMINOSITIES^a

Type	Number	LOG L _{3.6μm}			LOG L _{8.0μm}			LOG L _{24μm}		
		median	mean	rms	median	mean	rms	median	mean	rms
All Arp Disks	53	43.06	42.86	0.71	43.11	42.92	0.88	42.62	42.51	0.97
M51-like Disks	16	43.00	42.74	0.71	43.29	42.90	0.91	42.92	42.51	0.91
Tails/Bridges	30	41.92	41.76	0.54	41.71	41.73	0.69	41.29	41.39	0.80
Spirals	26	43.08	43.01	0.54	42.95	43.02	0.55	42.36	42.46	0.56
Irr/Sm	12	40.91	41.01	0.73	40.52	40.52	1.07	40.42	40.57	1.08

^aThese are 'monochromatic luminosities', νL_ν , in units of erg s^{-1} . For the 3.6 μm , 8.0 μm , and 24 μm bands, the effective frequencies used were 8.45×10^{13} Hz, 3.81×10^{13} Hz, and 1.27×10^{13} Hz, respectively. Upper limits were included in calculating the means and medians.

TABLE 8
STATISTICS ON SPITZER COLORS^{a,b}

Type	N	[3.6] – [4.5]			[4.5] – [5.8]			[5.8] – [8.0]			[3.6] – [8.0]			[8.0] – [24]			[3.6] – [24]		
		median	mean	rms	median	mean	rms	median	mean	rms									
Arp Disks	53	0.02	0.03	0.08	1.47	1.35	0.44	1.66	1.58	0.31	2.94	2.66	0.94	2.72	2.73	0.60	5.76	5.68	0.98
Wide Disks	27	0.01	0.01	0.06	1.55	1.38	0.51	1.73	1.61	0.35	2.94	2.56	1.12	2.74	2.58	0.48	5.81	5.56	1.12
Close Disks	42	0.02	0.03	0.08	1.43	1.34	0.40	1.64	1.56	0.30	2.97	2.73	0.80	2.65	2.81	0.65	5.67	5.75	0.89
M51-like	16	0.02	0.02	0.04	1.43	1.45	0.38	1.67	1.66	0.17	3.07	2.87	0.94	2.74	2.70	0.36	5.78	5.73	0.78
Tidal	30	0.01	0.01	0.10	1.54	1.48	0.50	1.56	1.46	0.36	2.59	2.48	0.82	3.48	3.33	0.59	6.19	6.26	0.58
Spirals	26	0.03	0.03	0.06	1.27	1.15	0.42	1.43	1.32	0.36	2.80	2.50	0.78	2.10	2.17	0.43	4.95	4.67	1.08
E/S0	4	0.01	0.24	0.46	0.75	1.01	0.73	1.10	0.98	0.57	1.89	2.23	1.52	2.69	2.76	0.91	4.58	4.99	2.41
Irr/Sm	12	0.11	0.10	0.07	0.43	0.67	0.46	0.97	1.06	0.37	1.53	1.86	0.81	3.22	3.47	0.82	4.62	5.09	1.20

^aUpper/lower limits are not included in these statistics. No color corrections were included.

^bFor comparison with these numbers, the mean [3.6] – [4.5], [4.5] – [5.8], [5.8] – [8.0], and [3.6] – [8.0] colors in the Whitney et al. (2004) field stars are –0.05, 0.1, 0.05, and 0.1, respectively, and the predicted values for interstellar dust are –0.35, 3.2, 2.1, and 4.95, respectively (Li & Draine 2001). The expected [8.0] – [24] color for dust varies from 2.6 – 4.3 (Li & Draine 2001), increasing with increasing interstellar radiation field intensity, while stars are expected to be at [8.0] – [24] ~0.0.

TABLE 9
KOLMOGOROV-SMIRNOV TEST RESULTS: PROBABILITY SAME PARENT SAMPLE^a

Samples	[3.6] – [4.5]	[4.5] – [5.8]	[5.8] – [8.0]	[3.6] – [8.0]	[8.0] – [24]	[3.6] – [24]
Arp Disks vs. Spirals	90.6	3.8 ^b	0.004 ^b / 0.3 ^c / 0.2 ^d	7.6 ^b	0.001 ^b / 0.001 ^c / 0.094 ^e	0.01 ^b / 0.30 ^c
Tails/Bridges vs. Spirals	18.7	3.3 ^b	19.9 ^b	81.5 ^b	<i>f</i>	<i>f</i>
M51-like vs. Spirals	91.7	7.2 ^b	0.01 ^b / 0.09 ^c / 0.04 ^e	7.9	0.01 ^b / 0.004 ^c / 0.02 ^e	0.4 ^b / 1.0 ^c
Close vs. Wide Pairs	56.2	61.5 ^b	10.2 ^b	14.5 ^b	21.7 ^b	38.9 ^b
Irr/Sm vs. Spirals	0.11	<i>f</i>	<i>f</i>	2.1 ^b / 4.1 ^c	<i>f</i>	46.1 ^b
Arp Disks vs. Arp Tails/Bridges	20.2	57.7 ^b	37.9 ^b	23.4 ^b	<i>f</i>	<i>f</i>
Arp Disks vs. Irr/ISm	0.005	<i>f</i>	<i>f</i>	<i>f</i>	<i>f</i>	<i>f</i>
Tails/Bridges vs. Irr/ISm	0.003	<i>f</i>	<i>f</i>	<i>f</i>	<i>f</i>	<i>f</i>

^aThe quoted numbers are percentages. Probabilities <1% mean it is highly probable that the two samples have different parent samples. Probabilities > 1% are inconclusive; we cannot rule out the hypothesis that the colors came from the same parent population.

^bUpper/lower limits are not included in these statistics.

^cUpper/lower limits are included as detections.

^dHalf of the lower limits are placed at the spiral peak, and half 0.2 dex lower.

^eUpper limits are placed at the peak of the spiral distribution.

^fToo few detections.